Depletion of CD206^{+} Tumour Macrophages via a Peptide-Targeted Star-Shaped Polyglutamate Inhibits Tumourigenesis and Metastatic Dissemination in Breast Cancer Models

Anni Lepland[¥,1], Alessio Malfanti[¥,2], Uku Haljasorg[3], Eliana K. Asciutto[4], Monica Pickholz[5,6], Mauro Bringas[7,8], Snežana Đorđević[2], Liis Salumäe[9], Pärt Peterson[3], Tambet Teesalu[ψ,1,10], María J. Vicent[ψ,2], Pablo Scodeller[ψ,1]

¥: equal contribution
ψ: equal contribution

[1] Laboratory of Precision and Nanomedicine, Institute of Biomedicine and Translational Medicine, University of Tartu, Ravila 14B, Tartu, 50411, Estonia

[2] Polymer Therapeutics Laboratory, Prince Felipe Research Centre, Av. Eduardo Primo Yúfera 3, Valencia 46012, Spain

[3] Molecular Pathology Research Group, Institute of Biomedicine and Translational Medicine, University of Tartu, Ravila 19, Tartu, 50412, Estonia

[4] School of Science and Technology, National University of San Martin (UNSAM) ICIFI and CONICET. Buenos Aires, Argentina.

[5] Departamento de Física, Facultad de Ciencias Exactas y Naturales, Universidad de Buenos Aires, Buenos Aires

[6] Instituto de Física de Buenos Aires (IFIBA), CONICET-Universidad de Buenos Aires, Buenos Aires, Argentina

[7] Departamento de Química Inorgánica, Analítica y Química Física, Facultad de Ciencias Exactas y Naturales, Universidad de Buenos Aires, Ciudad de Buenos Aires, C1428EHA, Argentina

[8] Fundación Instituto Leloir, Instituto de Investigaciones Bioquímicas de Buenos Aires (IIBBA-CONICET), C1405BWE Ciudad Autónoma de Buenos Aires, Buenos Aires, Argentina.

[9] Tartu University Hospital, Pathology department, Puusepa 8, 50406, Estonia

[10] Centre for Nanomedicine and Department of Cell, Molecular and Developmental Biology, University of California, Santa Barbara, 93106, CA, USA

Conflict of interest statement

PS and TT are inventors of patents on the mUNO peptide. MJV is an inventor of a patent on BTA-core branched polypeptides (including St-PGA) licensed to PTS SL. In addition, TT is an inventor of iRGD and CendR peptides and a shareholder of Cend Therapeutics Inc., a company that holds a license for the mUNO, iRGD and CendR peptides.

ABSTRACT

Although many studies have explored the depletion of tumour-associated macrophages (TAMs) as a therapeutic strategy for solid tumours, currently available compounds suffer from poor efficacy and dose-limiting side effects. Here, we developed a novel TAM-depleting agent ("OximUNO") that specifically targets CD206^{+} TAMs and demonstrated efficacy in triple negative breast cancer (TNBC) mouse models. OximUNO comprises a star-shaped polyglutamate (St-PGA) decorated with the CD206-targeting peptide mUNO that carries the chemotherapeutic drug doxorubicin (DOX). In TNBC models, a fluorescently labelled mUNO-decorated St-PGA homed to CD206^{+} TAMs within primary lesions and metastases. OximUNO exhibited no acute liver or kidney toxicity in vivo. Treatment with OximUNO reduced the progression of primary tumour lesions and pulmonary metastases, significantly diminished the number of CD206^{+} TAMs and increased the CD8/FOXP3 expression ratio (demonstrating immunostimulation). Our findings suggest the potential benefit of OximUNO as a TAM-depleting agent for TNBC treatment. Importantly, our studies also represent the first report of a peptide-targeted St-PGA as a targeted therapeutic nanoconjugate.

Keywords: polymer-drug nanoconjugates, targeting peptide, CD206, tumour-associated macrophages, triple negative breast cancer, pulmonary metastasis, immunomodulation

INTRODUCTION

Triple negative breast cancer (TNBC), defined by the lack of the expression of the oestrogen receptor (ER), progesterone receptor (PR), and human epidermal growth factor receptor 2 (HER2)[1,2], represents an aggressive breast cancer subtype with poor prognosis[3] that comprises up to 20% of all breast cancer cases[3,4]. Interfering with immune checkpoints signalling (e.g. through the modulation of programmed cell death 1 (PD-1) and its ligand (PD-L1)) represents an alternative treatment strategy for several cancers and is currently being employed in combination with chemotherapy as a neoadjuvant or adjuvant treatment[5–8]. The U.S. Food and Drug Administration (FDA) recently granted accelerated approval for a combination of a PD-L1 blocking antibody (atezolizumab, Tecentriq®) and nab-paclitaxel (Abraxane®)[9] as a first-line treatment for unresectable locally advanced or metastatic TNBC[10]. While promising clinical results have resulted, this combinatorial treatment approach suffers from significant obstacles, including the problematic identification and heterogeneity of PD-L1 expression in

patients[11], the limited applicability to PD-L1 positive TNBC patients (only 20–42% of cases)[12,13], and the induction of severe side effects (e.g., neutropenia, peripheral neuropathy, and colitis)[10,14,15]. Other immune checkpoint inhibitors (ICIs), including the cytotoxic T lymphocyte-associated antigen 4 (CTLA-4) blockers ipilimumab and tremelimumab, are currently under evaluation for TNBC treatment in combination with other drugs (clinical trial identifiers: NCT03606967, NCT02983045); however, anti-CTLA-4 treatments induce severe side effects such as endocrinopathies, myopathy, enterocolitis, and hepatitis[16–19], which narrow their use. Overall, the limited success of alternative treatment options for TNBC has maintained chemotherapy as the standard of care for most patients[20].

The anthracycline drug doxorubicin (DOX), which presents high off-target effects such as cardiotoxicity[21,22], represents a frequently employed chemotherapeutic for TNBC; however, disease relapse and metastatic development have also been associated with DOX treatment[23]. M2 (anti-inflammatory)-polarised tumour-associated macrophages (TAMs)[24] found within both primary and metastatic tumour lesions mediate both events[25]; furthermore, TAMs represent the main executioners of tumour progression, immunosuppression and invasion[24–29], and their presence correlates with inadequate therapeutic response and poor prognosis[25]. Recent efforts have focused on eliminating TAMs, and several ongoing clinical trials are currently evaluating TAM depletion in combination with treatments such as ICIs[30]. The current clinical-stage gold standard for TAM depletion relies on agents that block colony stimulating factor 1 (CSF1) or its receptor CSF1R, such as the small molecule CSF1R inhibitor PLX3397[31]; however, microglia also expresses CSF1R[32], the inhibition of CSF1R with PLX5622 impacts M1 macrophages[33], and PLX3397 treatment causes oedema[34]. Clinical data suggests that anti-CSF1R antibodies induce a modest effect[35,36] and cause severe side effects that include haematological toxicities[35] and hepatotoxicity by targeting Kupfer cells[35,36]. Overall, these findings highlight the overwhelming need for new TAM-depletion strategies.

Notably, both perivascular TAMs associated with disease relapse and therapeutic resistance[24] and metastasis-associated macrophages[37] express the mannose receptor (CD206/MRC1). Perivascular TAMs employ CD206 to navigate the surrounding collagen-dense stroma[38], which favours tumour progression[39,40].

For the first time, we report the effects of depleting the $CD206^+$ subpopulation of TAMs in metastatic TNBC mouse models through the use of a targeting agent (the mUNO peptide) for a CD206 site different from the mannose-binding site[41–44]. Previous studies have employed mannose to target CD206; however, mannose has other receptors besides CD206[45,46].

105 We decorated a three-arm branched biodegradable multivalent polyanion with a defined
106 negative charge and nanometre-size hydrodynamic radius (star-shaped polyglutamate or St-
107 PGA) with mUNO peptide to function as a targeted delivery platform for a chemotherapeutic
108 agent (DOX) conjugated through a bioresponsive linker. St-PGA-DOX-mUNO (referred to as
109 OximUNO) efficiently depleted $CD206^{+}$ TAMs, relieved immunosuppression in the tumour
110 microenvironment (TME) and limited metastasis/tumour growth, thereby supporting
111 OximUNO as an alternative TAM depletion strategy.
112 Most importantly, this study represents the first described combination of two reported
113 technologies – the St-PGA nanocarrier and the mUNO targeting peptide. Overall, this
114 OximUNO proof-of-concept demonstrates the potential of the peptide-targeted St-PGA
115 nanosystem. Our studies lay a foundation for future work using this nanosystem to target other
116 receptors efficiently by changing the targeting peptide.
117
118
119 **RESULTS**
120 **Design and structural modelling of St-PGA-OG-mUNO**
121 To characterise and explore the function of OximUNO, we first developed an mUNO-targeted
122 St-PGA labelled with the Oregon Green (OG) fluorescent dye (referred to as St-PGA-OG-
123 mUNO) (Fig. 1A, Scheme S1). We conjugated OG to St-PGA using an amide linker to allow
124 in vitro or in vivo tracking and coupled mUNO through a disulphide bond formed between the
125 free cysteine of mUNO and a pyridyldithiol linker on St-PGA. We previously demonstrated
126 that mUNO conjugated to polymeric nanostructures through the cysteine thiol group preserves
127 CD206 binding[42]. To evaluate the structure and dye loading, we analysed St-PGA-OG-mUNO
128 and St-PGA-OG using nuclear magnetic resonance (NMR) and UV-Vis analyses (Fig. S1).
129 Dynamic light scattering (DLS) analysis demonstrated that St-PGA-OG-mUNO and St-PGA-
130 OG displayed similar hydrodynamic diameters of 6.8 and 5.9 nm, respectively (Fig. 1B, C),
131 while both nanoconjugates exhibited highly negative charges (-42 mV and -48 mV,
132 respectively) as shown by Zeta potential analysis (Fig. 1B); an expected result given the
133 glutamic acid nature of the polymer carrier. Analysis of mUNO loading (Fig. 1B) indicated the
134 presence of approximately seven mUNO peptides in St-PGA-mUNO nanoconjugate, which
135 would allow multivalent receptor binding.
136 We next assessed the structure of unlabelled and untargeted St-PGA in water using molecular
137 dynamics (MD) simulations to access information at the atomic scale. We assumed an initial

138 helical conformation for the three PGA chains. The studied system consisted of a fully hydrated
139 St-PGA and the Na^+ counterions (~920,000 atoms) and was built after initial minimisation
140 under vacuum conditions. We simulated 50 ns of the entire St-PGA macromolecule, with Fig.
141 1D displaying a snapshot corresponding to the last step of the simulation. Averaging the
142 gyration radius over the last 25 ns of the simulation run provided a value of 5.6 ± 0.3 nm, which
143 lies in the same order of magnitude as the results from DLS analysis and suggests a lack of
144 aggregation of both St-PGA-OG-mUNO and St-PGA-OG in PBS. A video simulation (Video
145 S1) suggested that the three PGA chains remain in an extended conformation throughout the
146 simulation and do not show any intra- or inter-molecular interaction, suggesting that the mUNO
147 peptides linked to St-PGA will not interfere with each other.
148 To investigate if mUNO can engage with the CD206 receptor when grafted onto St-PGA, we
149 modelled the structure and mobility of St-PGA-mUNO using computational analysis. To attain
150 a computationally feasible system, we simulated only single branches of St-PGA-mUNO. We
151 placed three equidistant mUNO peptides on a PGA single branch and fully solvated the system.
152 We observed that three mUNO peptides remained exposed to the solution available for receptor
153 binding (Fig. 1E). The rotation of mUNO around PGA, tracked by the angle formed by a
154 proline aromatic carbon within mUNO (Fig. S2, green sphere), a pyridyldithiol linker nitrogen
155 (Fig. S2, blue sphere), and a glutamic acid aromatic carbon (Fig. S2, light blue sphere) revealed
156 angles between 50º and 180º (Fig. 1F). This value supports the ability of mUNO peptides to
157 interact with their receptor[43]. Comparisons with an undecorated PGA branch demonstrated the
158 minimal alterations of secondary structure dynamics in the presence of mUNO peptides -
159 turning alpha helices (Fig. 1G, green) into random coils (Fig. 1G, brown) at regions where they
160 are placed; however, the PGA chain structure remained mainly helical except in the middle,
161 where a slight kink formed (Fig. 1G).
162

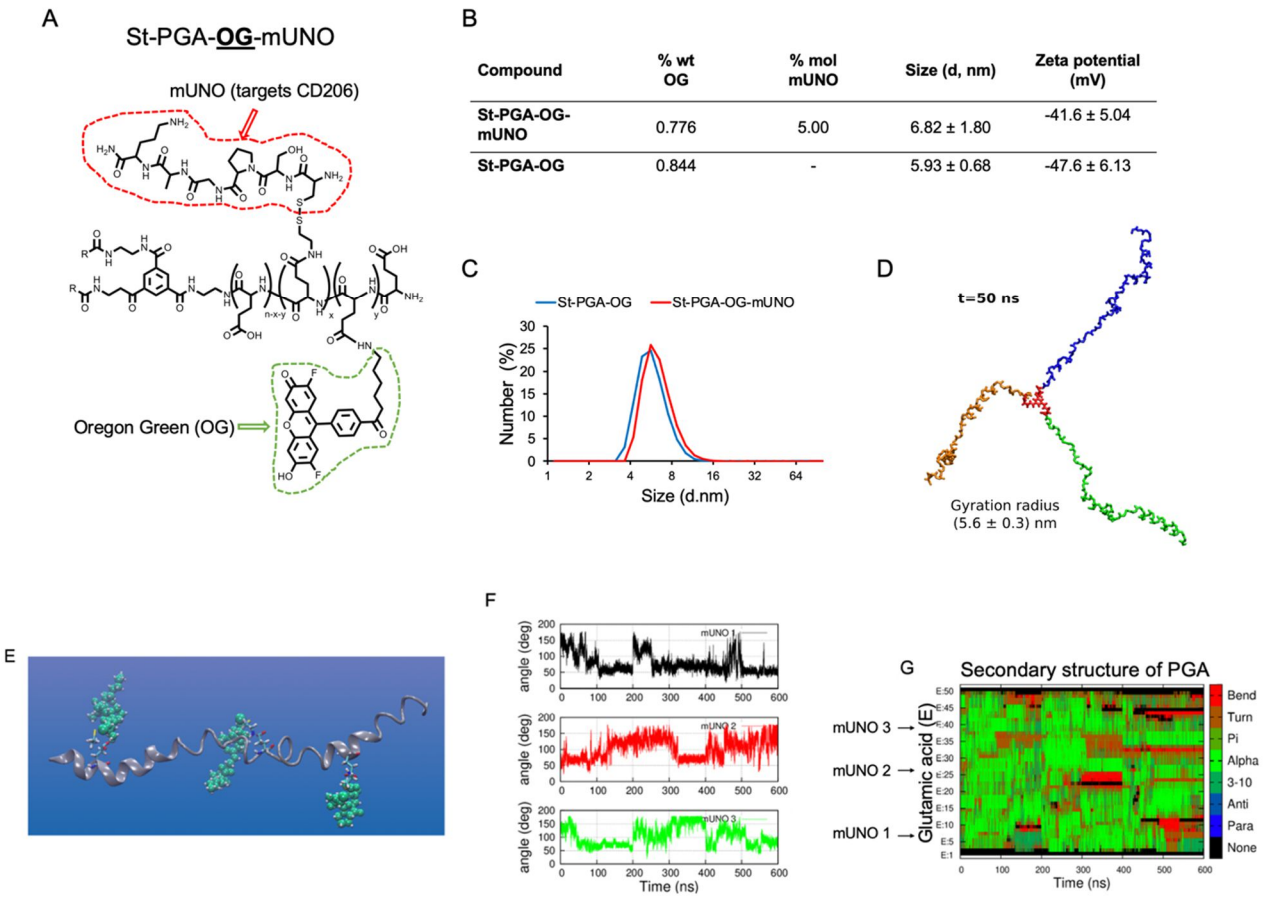

Compound	% wt OG	% mol mUNO	Size (d, nm)	Zeta potential (mV)
St-PGA-OG-mUNO	0.776	5.00	6.82 ± 1.80	-41.6 ± 5.04
St-PGA-OG	0.844	-	5.93 ± 0.68	-47.6 ± 6.13

Figure 1. Design and analysis of mUNO-targeted St-PGA. (**A**) Representative structure of St-PGA decorated with mUNO peptides (red) and OG (green). (**B**) Table detailing OG loading, mUNO loading, size (as measured by DLS), and charge (as measured by Zeta potential analysis). (**C**) DLS graph demonstrating uniform size for both St-PGA-OG-mUNO and St-PGA-OG. (**D**) A snapshot of modelled St-PGA structure in water and Na^+ counterions at the last stage of the simulation (50 ns), displaying the three arms in different colours for visual clarity. The average gyration radius was 5.6 ± 0.3nm, t shows time in ns. (**E**) Representative MD snapshot of a single St-PGA-mUNO branch containing three equidistant mUNO peptides. Green spheres represent mUNO and a Licorice representation shows the linker. (**F**) mUNO rotation around the PGA chain for each of the three peptides (black, red, and green lines). (**G**) PGA chain secondary structure evolution, where red and brown regions show how mUNO perturbs the chain structure, turning alpha helices into random coils.

Altogether, St-PGA-OG-mUNO and St-PGA-OG nanoconjugates possessed similar sizes by DLS, highly negative charges, and, according to simulations, displayed their three arms in an extended open structure. Our simulation analyses demonstrated that mUNO peptides induced a minimal effect on PGA structure and rotated around the PGA chain with considerable freedom. Overall, these findings suggest St-PGA-mUNO as a suitable platform for CD206 targeting.

182 **St-PGA-OG-mUNO targets CD206$^+$ TAMs and displays low hepatic accumulation**

183 We next evaluated the potential of St-PGA-OG-mUNO to target CD206$^+$ TAMs in two
184 different TNBC models – an orthotopic TNBC model and an experimental metastasis of TNBC
185 model induced by intravenous (i.v.) injection of 4T1 cells. We administered St-PGA-OG-
186 mUNO or St-PGA-OG intraperitoneally (i.p.), allowed circulation for 6 h, and then analysed
187 tumour homing using confocal fluorescence microscopy. Our previous study provided the
188 rationale for the i.p. administration route, where we demonstrated that the i.p. administered
189 mUNO peptide exhibited a substantially longer half-life than i.v. administered mUNO in the
190 same mice (same strain, sex and age) used in this study[42].

191 In the orthotopic TNBC model, we observed a high colocalisation of OG/CD206 (Fig. 2A,
192 yellow signal) with St-PGA-OG-mUNO but a much lower colocalisation of OG/CD206 with
193 non-targeted St-PGA-OG (Fig. 2B) (0.57 and 0.21, respectively (Fig. 2M)). We observed a low
194 level of accumulation of St-PGA-OG-mUNO or St-PGA-OG in the liver (Fig. S3A, B). We
195 employed confocal image acquisition parameters throughout this study to visualise CD206 in
196 the tumour without signal saturation. Given the higher levels of CD206 in the tumour, imaging
197 with associated settings provides low CD206 visualisation in the liver. Using a higher image
198 intensity, we observed the expected CD206 signal in the liver (as expected from Kupfer cells
199 and sinusoid vessels) (Fig. S4A) and a saturated CD206 signal in the tumour (Fig. S4B).

200 Immunostaining for endogenous mouse IgG in the tumour and the liver indicated the leaky
201 nature of the tumour vasculature (Fig. S5A) compared to the liver vasculature (Fig. S5B) in the
202 4T1 model. A leaky tumour vasculature favours the hypothesis that St-PGA-OG-mUNO has a
203 more extended (both in time and space) access to CD206 in the tumour than in the liver. We
204 speculate that the leaky tumour vasculature combined with lower CD206 expression in the liver
205 than the tumour explains the low hepatic accumulation of St-PGA-OG-mUNO. St-PGA-OG-
206 mUNO did not accumulate in the lungs (Fig. S6A) or spleen (Fig. S6B); however, we did
207 observe some accumulation in the sentinel lymph node (SLN) (Fig. S6C) and the kidneys (Fig.
208 S6D). Of note, the observed kidney signal agrees with our prior studies that demonstrated the
209 renal excretion of St-PGA[47].

210 Importantly, we did not detect homing to M1 macrophages (CD86$^+$) or dendritic cells (CD11c$^+$,
211 DCs) with St-PGA-OG-mUNO (Fig. 2C, E) or with St-PGA-OG (Fig. 2D, F). In the
212 experimental metastasis of TNBC model, most of the cellular signal of St-PGA-OG-mUNO
213 associated with CD206$^+$ TAMs (Fig. 2G, yellow signal) when compared to St-PGA-OG (Fig.
214 2H) (OG/CD206 colocalisation 0.42 and 0.14, respectively, Fig. 2N). In this model, we also

215 observed no colocalisation between OG and CD86 (M1 macrophages) (Fig. 2I, J) or OG and
216 CD11c (DCs) (Fig. 2K, L) and the observed hepatic accumulation of St-PGA-OG-mUNO or
217 St-PGA-OG was low (Fig. S7).
218 One of the rationales behind the design of OximUNO was to increase mUNO targeting through
219 increased avidity and plasma half-life. To evaluate these aspects, we compared the homing of
220 St-PGA-OG-mUNO with a monomeric, carboxyfluorescein-labelled mUNO peptide (FAM-
221 mUNO). We note that even given the different nature of the fluorescent labels (OG on St-PGA-
222 OG-mUNO and fluorescein on FAM-mUNO), we did not use their native fluorescence as a
223 readout; instead, we used an antibody that recognises both FAM and OG; therefore, we do not
224 expect biases from potential differences in FAM and OG emissions.
225 We discovered that St-PGA-OG-mUNO (Fig. S8A) displayed significantly higher OG/CD206
226 colocalisation than for FAM/CD206 with FAM-mUNO (Fig. S8B) at 6 h (0.74 vs. 0.21,
227 respectively (Fig. 2O)). Additionally, we found that the OG/FAM mean signal per $CD206^{+}$ cell
228 was five times higher for St-PGA-OG-mUNO than FAM-mUNO (Fig. 2P). These findings
229 suggest that conjugating mUNO to the St-PGA backbone greatly improved receptor binding.
230 Plasma half-life analysis for i.p. administered St-PGA-OG-mUNO revealed a 4.5 h half-life
231 (Fig. 2Q), a value over two times longer than that observed after the i.p. administration of
232 FAM-mUNO in our previous study[42]. Overall, this finding suggests that conjugating peptide
233 onto St-PGA increased the plasma half-life of mUNO peptide, a desirable feature that will
234 improve in vivo ligand targeting.
235 We next compared tumour homing of St-PGA-OG-mUNO to that of a therapeutic monoclonal
236 antibody by i.v. injecting anti-PDL1 in orthotopic 4T1 tumour-bearing mice and allowing
237 circulation for 24 h. We observed that administered anti-PDL1 accumulated in the tumour rim
238 (Fig. 2R, TR) but not in the tumour core (Fig. 2R, TC) even given expression of the receptor
239 (PDL1) in the tumour core (Fig. 2S, TC). The observed accumulation of St-PGA-OG-mUNO
240 in the tumour core (Fig. 2T, TC) and receptor colocalisation (Fig. 2U), supported the
241 implementation of our platform as an efficient alternative to antibody-based therapies such as
242 anti-PDL1 or antibody-drug conjugates.

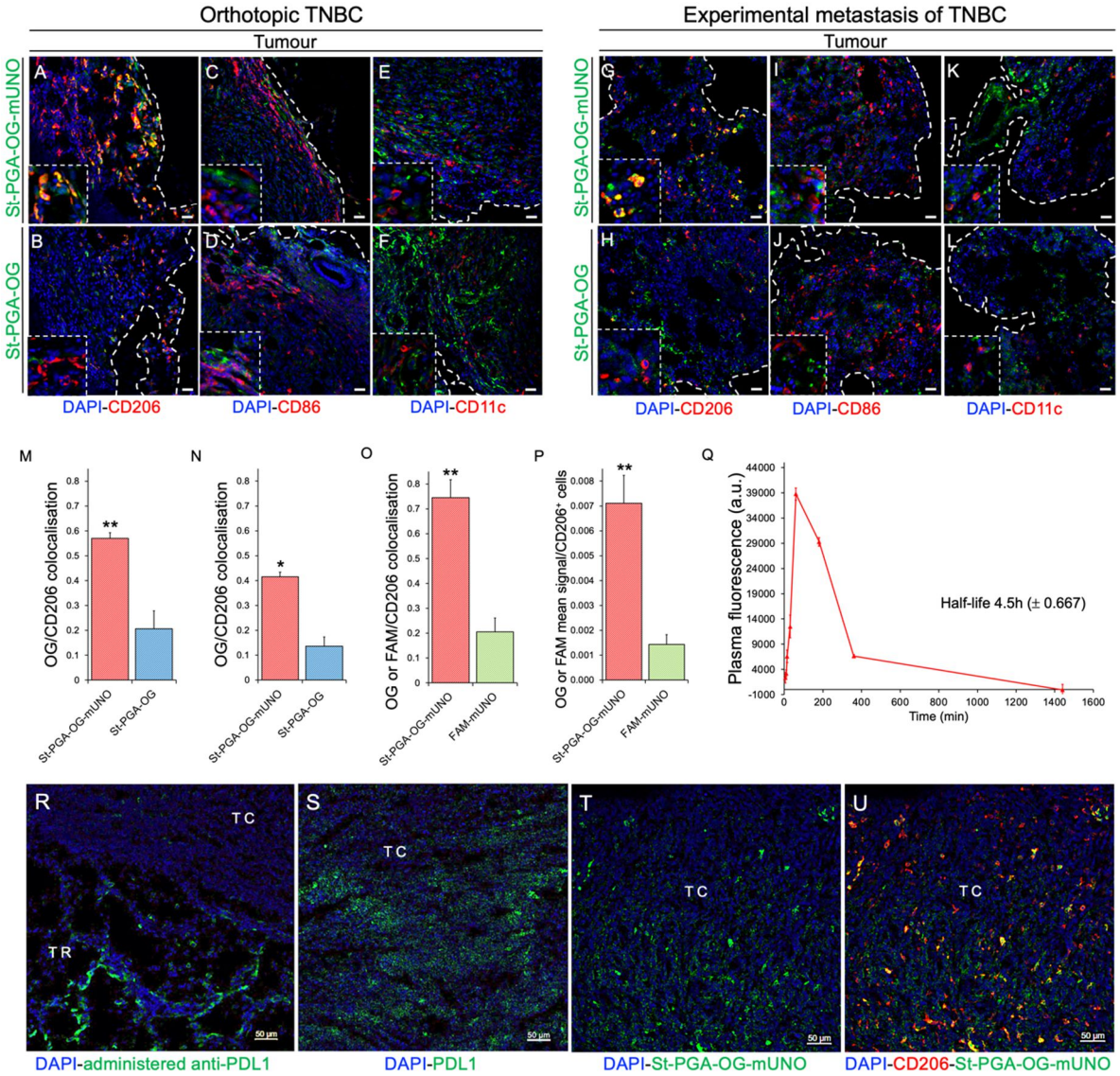

Figure 2. St-PGA-OG-mUNO targets CD206⁺ TAMs in models of orthotopic TNBC and experimental metastasis of TNBC and displays an extended plasma half-life. Homing studies with i.p. administered St-PGA-OG-mUNO (0.41 mg/0.5mL of PBS) or St-PGA-OG (0.35 mg/0.5mL of PBS), after 6 h of circulation. N=3 for orthotopic TNBC and N=2 for experimental metastasis of TNBC. (**A-F**) Homing in orthotopic TNBC. (**A**) St-PGA-OG-mUNO displayed high colocalisation between OG and CD206 (yellow signal), whereas (**B**) St-PGA-OG displayed minimal colocalisation. St-PGA-OG-mUNO and St-PGA-OG did not show any homing to (**C, D**) CD86⁺ cells (M1 macrophages) nor (**E, F**) CD11c⁺ cells (DCs). (**G-L**) Homing study in the experimental metastasis of TNBC. (**G**) St-PGA-OG-mUNO displayed high colocalisation with OG and CD206 (yellow signal), whereas (**H**) St-PGA-OG showed minimal colocalisation. St-PGA-OG-mUNO and St-PGA-OG did not show any homing to (**I, J**) CD86⁺ cells (M1 macrophages) or (**K, L**) CD11c⁺ cells (DCs). Scale bars = 20 µm. (**M**) Graphs depicting the quantification of CD206 and OG colocalisation in the orthotopic TNBC and (**N**) the experimental metastasis of TNBC. (**O**) Quantification of colocalisation analysis for St-PGA-OG-mUNO or FAM-mUNO with CD206 homing after 6 h of circulation, N=2 (30 nmoles in OG and FAM, respectively). Colocalisation was quantified using the Fiji programme and Pearson's coefficient (for more information see Materials and methods). (**P**) Mean OG/FAM signal per CD206⁺ cell analysed using the ImageJ programme. (**Q**) Plasma fluorescence (in

259 the green channel) of i.p. administered St-PGA-OG-mUNO (dose 15 nmoles in OG) in healthy Balb/c mice (N=3).
260 (**R**) Rat anti-mouse PDL1 was i.v. injected ten days post tumour induction (p.i.) and circulated for 24 h after which
261 time, mice were sacrificed, tumours collected, fixed, and stained for PDL1. **(S)** PDL1 expression was detected in
262 s.c. 4T1 tumours by staining with rat anti-mouse PDL1. (**T, U)** Representative images showing St-PGA-OG-
263 mUNO (0.41mg/0.5mL) i.p. injected ten days post tumour induction and circulated for 6 h after which time, mice
264 were sacrificed, tumours fixed, and then stained for OG and CD206. The OG channel is shown separately in **(T),**
265 and the colocalisation with CD206 for the same image is shown in **(U).** Scale bars = 50 µm. TC: tumour core, TR:
266 tumour rim**.** Error bars represent the standard error (SE) of the mean.
267
268 Administration of a higher dose of both nanoconjugates (0.82 mg/0.5mL St-PGA-OG-mUNO
269 and 0.7 mg/0.5mL St-PGA-OG) resulted in high CD206$^+$ TAM targeting (Fig. S9A) albeit at
270 the expense of higher hepatic accumulation (Fig. S9C). For this reason, we employed lower
271 nanoconjugate doses (0.41 mg/0.5mL and 0.35 mg/0.5mL) for subsequent studies.
272
273 Overall, we demonstrated that St-PGA-OG-mUNO, homes to CD206$^+$ TAMs in both
274 orthotopic and experimental metastasis of TNBC models with no significant hepatic
275 accumulation. We also established that St-PGA-OG-mUNO does not target M1 macrophages
276 or DCs in the tumour, thereby providing evidence of high specificity for CD206$^+$ TAMs.
277
278
279 **OximUNO enhances the in vitro cytotoxicity of DOX on M2 macrophages**
280 St-PGA displays a large surface with multiple sites available for the conjugation of pro-
281 apoptotic or cytotoxic cargoes via bioresponsive polymer-drug linkers[48,49]. To selectively
282 deplete CD206$^+$ TAMs, we conjugated an apoptotic chemotherapeutic agent (DOX) to St-
283 PGA-mUNO to form St-PGA-DOX-mUNO (designated "OximUNO") (Fig. 3A, Scheme S2).
284 We conjugated DOX to St-PGA-mUNO using a hydrazone bond[48] to allow for site-specific
285 drug release in the acidic milieu of the endosomes/lysosomes[48,50].
286 To evaluate the effect of mUNO targeting, we included St-PGA-DOX as an untargeted control.
287 We employed ^{1}H NMR and UV-Vis analyses to evaluate the chemical identity of
288 nanoconjugates (Fig. S10A, B).
289 OximUNO displayed DOX and mUNO loadings of ~10% and ~4% in weight, respectively,
290 corresponding to around four DOX and seven mUNO molecules for every OximUNO.
291 OximUNO exhibited a size of ~40 nm and a highly negative surface charge of -40 mV (Fig.
292 3B, C). We obtained similar DOX loading, size by DLS, and surface charge values for St-PGA-
293 DOX (Fig. 3B, C).

294 The pH-sensitive hydrazone linker and the intrinsic biodegradability of St-PGA by lysosomal
295 protease cathepsin B are expected to secure DOX release from OximUNO after cell
296 internalisation[51]. Hence, we studied DOX release kinetics from OximUNO in the presence of
297 acidic pH (pH 5) and cathepsin B using liquid chromatography-mass spectrometry (LC-MS,
298 Fig. S11A-G). As we aimed for the i.p. administration of OximUNO, we assessed DOX release
299 in intraperitoneal fluid (i.p. fluid) (Fig. 3D). At pH 5, we observed a sustained DOX release in
300 the first 8 h (reaching a plateau at 15%), thereby demonstrating the suitability for endo-
301 lysosomal drug delivery. DOX release in the presence of cathepsin B displayed comparable
302 values in the first 8 h (~13%), followed by a plateau and a reduced rate in the following hours
303 (~13% cumulative release at 72 h). Importantly, OximUNO exhibited negligible drug release
304 in both physiological conditions evaluated (PBS and i.p. fluid) (Fig. 3D).
305 We next evaluated the in vitro cytotoxicity of OximUNO and St-PGA-DOX in primary human
306 blood monocyte-derived M2, M0 and M1 macrophages. Since the in vivo concentration that
307 provided optimal $CD206^{+}$ TAM targeting with minimal hepatic accumulation was 30 μM in
308 OG, here we focused our interest on conjugates at 33 μM of DOX. Our previous studies
309 comparing other mUNO-targeted vs. untargeted polymeric nanosystems[44] demonstrated that
310 the highest targeted uptake in primary M2 macrophages occurred after an interval of 10 to 30
311 min. For this reason, we used an incubation time of 15 min for these experiments.
312 Importantly, in M2 macrophages, OximUNO displayed a significantly higher toxicity than
313 DOX and St-PGA-DOX (Fig. 3E). Since CD206 is expressed on macrophage populations in
314 other organs, although at lower levels than for M2 TAMs, we also evaluated the effect on non-
315 polarised, "M0", macrophages, which we previously showed express CD206 at levels lower
316 than in M2 macrophages[42]. OximUNO revealed a moderate toxicity to M0 macrophages (Fig.
317 3F), but lower than the toxicity to M2. Despite this moderate toxicity, as St-PGA-OG-mUNO
318 did not target the lung, liver, or spleen (Fig. S6), we expect OximUNO not to affect the
319 macrophage populations of those organs. St-PGA-DOX showed its highest toxicity in M1
320 macrophages (Fig. 3G). We speculate that here, the phagocytic activity, known to be highest
321 for M1 macrophages[52,53], governs the uptake and also explains the 60% cell viability observed
322 for OximUNO (Fig. 3G). In vivo, St-PGA-OG-mUNO did not target M1 TAMs (Fig. 2C, I),
323 hence, we do not expect OximUNO to affect this population. Free DOX only displayed toxicity
324 in M2 macrophages at 100 μM (Fig. 3E).
325 These results provide evidence that OximUNO displayed increased toxicity towards M2
326 macrophages when compared to St-PGA-DOX or DOX alone.
327

We also evaluated the hepatic and renal safety profile of a single administration of OximUNO (at doses corresponding to 2 mg/kg and 4 mg/kg of DOX) by analysing creatinine (Crea) and alanine aminotransferase (ALAT) levels 48 h after i.p. administration in healthy mice (Fig. 3H). These doses did not induce toxic levels of Crea or ALAT compared to the values reported in the literature[54] or the reference values for the female Balb/c reported in the Mouse Phenome Database by The Jackson Laboratory[55] or Charles River facilities[56]. However, increased ALAT levels with the higher dose, prompted the selection of the OximUNO dose corresponding to 2 mg/kg of DOX for further in vivo studies.

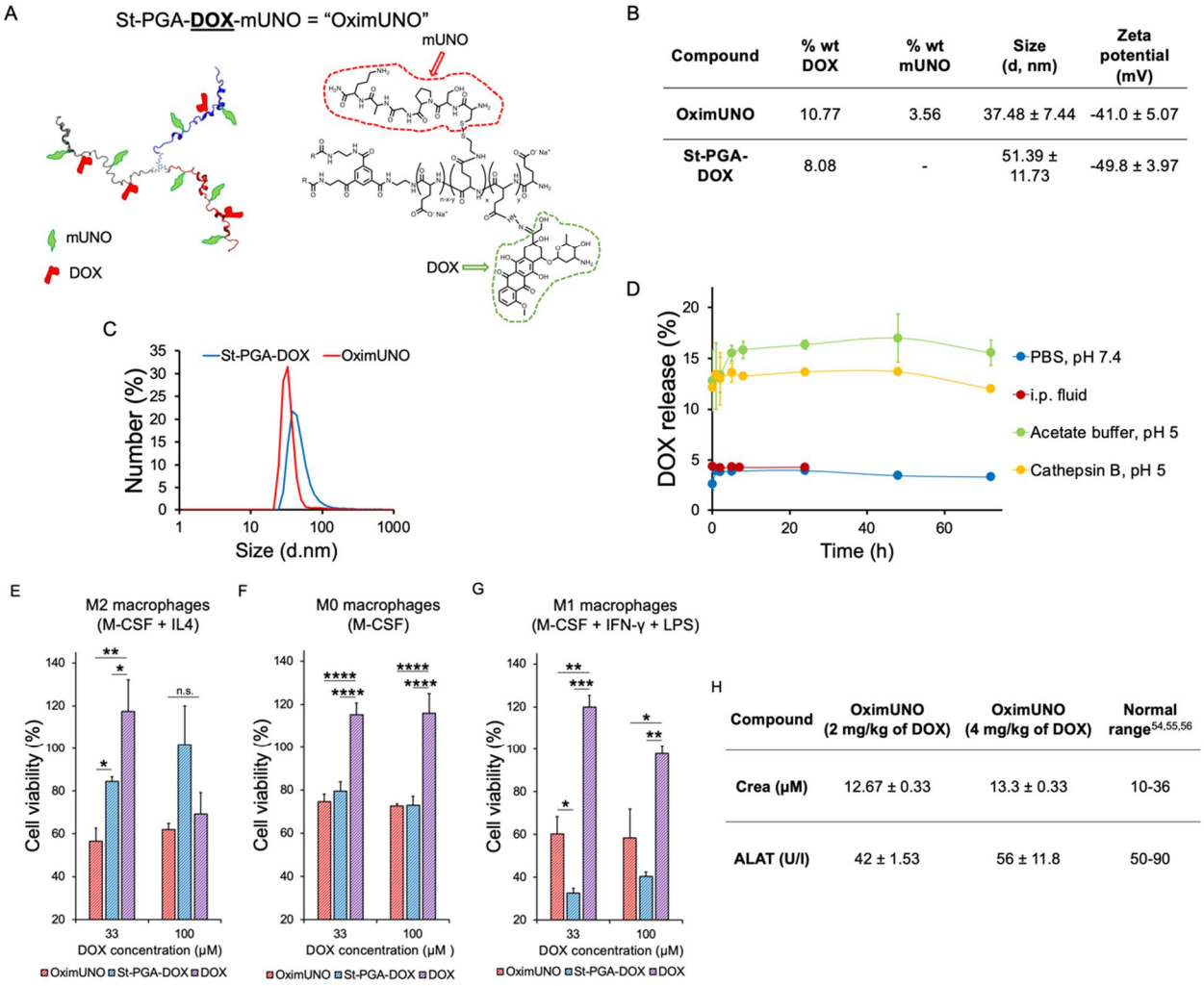

Figure 3. OximUNO enhances the in vitro efficacy of DOX on M2 macrophages. (**A**) Simplified form of OximUNO (left) and molecular structure (right) showing St-PGA decorated with mUNO (red) and DOX (green). (**B**) Table showing DOX loading, mUNO loading, size (as measured by DLS), and charge (as measured by Zeta potential) of both nanoconjugates in PBS. (**C**) A DLS graph for measurements shown in (B), indicating the uniform size of OximUNO and St-PGA-DOX. (**D**) DOX release from OximUNO showing the drug release in PBS, i.p. fluid, acetate buffer or in the presence of cathepsin B. (**E-G**) In vitro cytotoxicity in primary human (**E**) M2, (**F**) M0, or (**G**) M1 macrophages after treatment with OximUNO (red bars), St-PGA-DOX (blue bars), and

345 DOX (purple bars) following a 15 min incubation, washed, cultured for additional 48 h, and then analysed for cell
346 viability as evaluated by MTT assay. (**H**) Hepatic and renal toxicology serum levels of Crea and ALAT 48 h after
347 i.p.-administration of OximUNO (at two different doses in DOX: 2 mg/kg and 4 mg/kg) in healthy Balb/c mice
348 (N=3). Error bars represent the SE of the mean.
349
350 In summary, the conjugation of mUNO and DOX to the St-PGA backbone to yield OximUNO,
351 enhanced the in vitro efficacy of DOX towards M2 macrophages with no in vivo renal or
352 hepatic toxicity observed.
353

354 OximUNO treatment of orthotopic TNBC depletes CD206$^+$ TAMs, inhibits 355 tumour progression and attenuates immunosuppression

356 The findings of the in vivo homing and in vitro cytotoxicity studies supported the subsequent
357 evaluation of OximUNO in the orthotopic TNBC model. When tumours reached 25 mm^3, we
358 treated mice with i.p. injections of OximUNO, St-PGA-DOX, or DOX, at 2 mg/kg of DOX
359 every other day for eighteen days. Encouragingly, OximUNO treatment significantly reduced
360 primary tumour volume growth kinetics (Fig. 4A, red line) compared to DOX, St-PGA-DOX,
361 and PBS. Furthermore, only the OximUNO treatment significantly reduced final tumour
362 weight (Fig. 4B) compared to the untreated group. We assigned this encouraging therapeutic
363 effect to mUNO-mediated targeting, as animals treated with the untargeted St-PGA-DOX
364 possessed tumour volumes (Fig. 4A, blue line) similar to the PBS group (Fig. 4A, black line).
365 Furthermore, OximUNO treatment did not affect mouse bodyweight, whereas treatment with
366 DOX induced a significant decrease in mouse bodyweight starting from day twenty-one p.i.
367 until the end of the treatment (Fig. 4C).
368 Histological analysis of lungs from treated mice (Fig. S12 shows an H&E stain from a healthy
369 lung for comparison) revealed that OximUNO also influenced the extent of pulmonary
370 metastases (Fig. 4D), as it elicited the highest reduction in the metastatic lung area and nodule
371 number ($p=0.06$ vs. PBS and $p=0.06$ vs. DOX, respectively (Fig. 4E, F)). Meanwhile,
372 immunofluorescence (IF) microscopy revealed no significant changes in CD31 expression in
373 tumours (Fig. 4G, H), but significantly fewer CD31$^+$ structures in the OximUNO-treated mice
374 compared to DOX-treated mice (Fig. 4G, I), suggesting that the reduction in nodule number in
375 the OximUNO group (of Fig. 4F) may be mediated by the lower vascularisation in the primary
376 tumour. Importantly, histological analysis revealed no cardiotoxicity in any treatment groups
377 (Fig. S13). IF analysis revealed that only OximUNO significantly reduced the CD206
378 expression (assigned to CD206$^+$ TAMs), compared to PBS (Fig. 4J, M). Interestingly,

379 treatment with DOX upregulated CD206 expression (Fig. 4J, M), which agrees with previous
380 reports that demonstrated an increase in the number of $CD206^{+}$ TAMs following
381 chemotherapy[24].
382 Notably, only OximUNO treatment significantly increased CD8 expression (a marker of
383 cytotoxic T cells (CTLs)) compared to PBS and DOX treatment (Fig. 4K, N). Unexpectedly,
384 St-PGA-DOX treatment increased the expression of FOXP3, a marker for regulatory T cells
385 (Tregs) (Fig. 4L, O). Analysis of the CD8/FOXP3 expression ratio revealed that OximUNO
386 treatment resulted in a five-fold increase compared to St-PGA-DOX or DOX treatment (Fig.
387 4P), suggesting that OximUNO stimulated a shift in the immune landscape towards
388 immunostimulation. Of note, in all cases, we normalised the quantification of marker
389 expression using immunofluorescent images to the tissue area to account for different amounts
390 of tissue in different images.

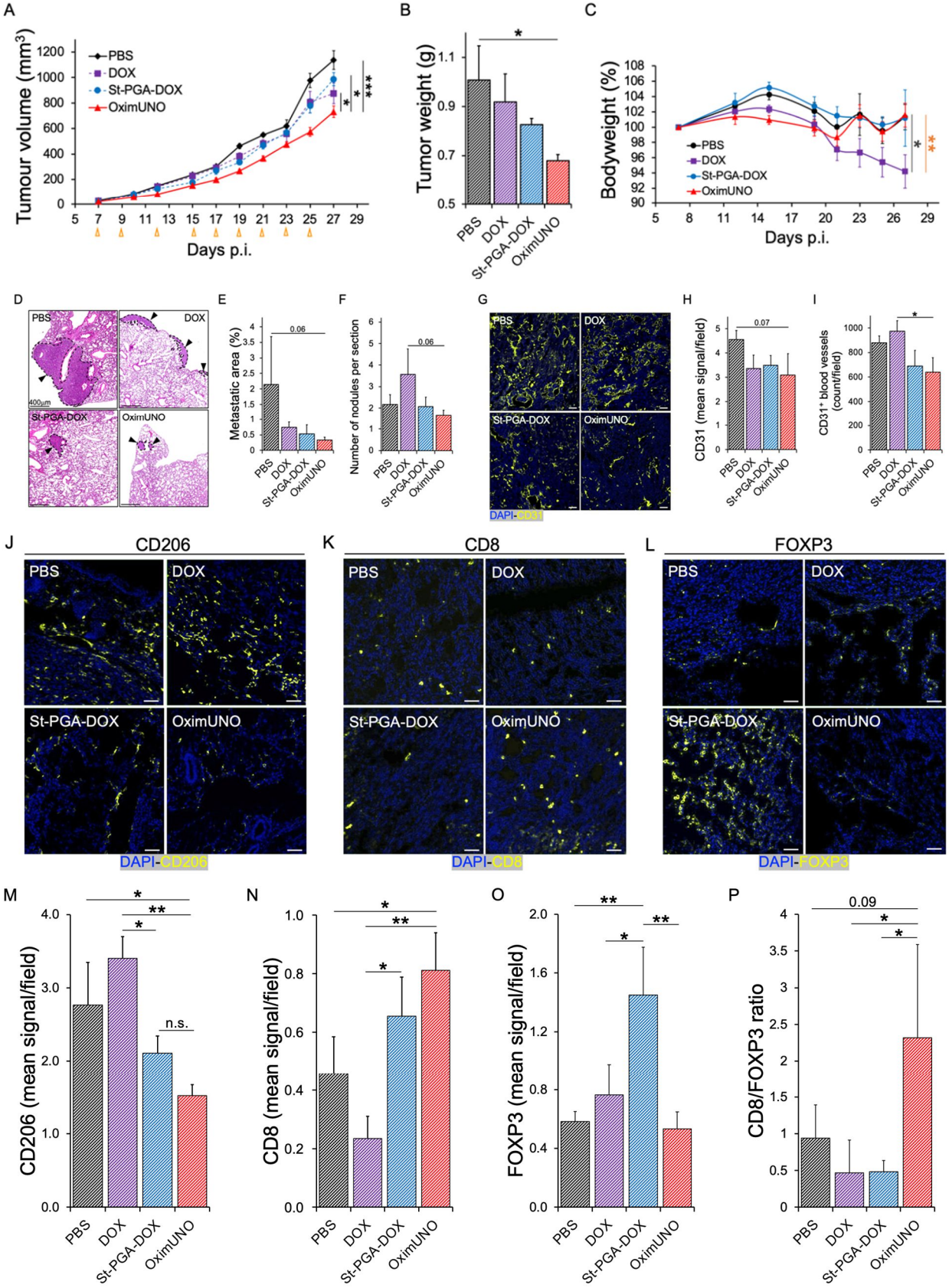

Figure 4. OximUNO treatment reduces primary tumour growth and pulmonary metastases and alleviates immunosuppression. Treatment with OximUNO, St-PGA-DOX, or DOX at 2 mg/kg of DOX in mice bearing orthotopic TNBC tumours (N=5). I.p. injections began when tumours reached 25 mm^3 and were performed every

395 other day to give a total of nine injections. (**A**) Primary tumour volume progression during treatment. Orange
396 arrows indicate injection days. (**B**) Primary tumour weight at the experimental endpoint, demonstrating a
397 significantly smaller weight for OximUNO-treated mice (red bar) than other groups. (**C**) Mouse bodyweight
398 analysis suggests the safety of OximUNO treatment (red line); meanwhile, DOX-treatment induced a significant
399 reduction in bodyweight by the experimental endpoint (purple line). Dark grey ∗ DOX vs. PBS, orange ∗ DOX
400 vs. St-PGA-DOX. (**D**) Representative H&E images showing pulmonary metastases for all groups (scale bars =
401 400 μm); OximUNO treatment associated with (**E**) the smallest metastatic area and (**F**) the lowest number of
402 average nodules per lung. **(G)** Representative images showing the expression of CD31 and blood vessels. **(H)**
403 Graph depicting the expression of CD31. **(I)** Graph depicting the $CD31^+$ blood vessel count. CD31 expression
404 and blood vessel count were calculated using ImageJ and five images per mouse per group for expression analysis
405 and at least three images per mouse per group for blood vessel count. (**J-L**) Representative confocal microscopy
406 images demonstrating the expression of (**J**) CD206, (**K**) CD8, and (**L**) FOXP3. Scale bars = 50 μm. (**M-P**)
407 Quantification of confocal microscopy images for the expression of (**M**) CD206, (**N**) CD8, and (**O**) FOXP3. (**P**)
408 Graph of CD8/FOXP3 expression ratio showing a shift in the immune profile. Quantification was performed using
409 the ImageJ programme from at least three images per mouse and five mice per group. Error bars represent the SE
410 of the mean.
411
412 By targeting $CD206^+$ TAMs with DOX via OximUNO treatment, we increased the efficacy
413 and reduced the toxicity of DOX in the orthotopic TNBC model. Our results also suggest that
414 the depletion of $CD206^+$ TAMs by OximUNO elicited an immunostimulatory shift.
415
416
417 **OximUNO treatment of experimental TNBC metastasis reduces $CD206^+$ TAMs**
418 **number, tumour burden and attenuates immunosuppression**
419 We next evaluated the effect of OximUNO on experimental TNBC metastasis using GFP-
420 labelled 4T1 cells. We treated mice every other day with i.p. injections of OximUNO, St-PGA-
421 DOX, or DOX, starting from day four p.i. and sacrificed mice on day eighteen p.i. Analysis of
422 whole lung fluorescence in the green channel revealed that OximUNO treatment induced the
423 lowest GFP fluorescence, indicating a lower level of pulmonary metastases (Fig. 5A).
424 Representative macroscopic images also provided evidence for a reduction in metastases (Fig.
425 5B). Confocal fluorescence microscopy of lungs confirmed the trend observed with whole lung
426 fluorescence, showing fewer GFP fluorescent nodules in the OximUNO-treated group (Fig.
427 5C). Furthermore, histological analysis of lungs displayed the lowest number of pulmonary
428 nodules for OximUNO-treated mice (Fig. 5D). Mice treated with the untargeted St-PGA-DOX
429 and free DOX showed a significant decrease in bodyweight, resulting in a 19% (Fig. 5E, blue

line) and 17% loss (Fig. 5E, purple line), respectively; meanwhile, OximUNO-treated mice displayed lower bodyweight loss (Fig. 5E, red line).

We next employed flow cytometry (FC) to analyse the effect of different treatments on the immune cell populations in whole lungs. This analysis demonstrated that OximUNO treatment significantly lowered the percentage of M2 TAMs ($CD206^+$) (Fig. 5F) but did not significantly impact the percentage of M1 TAMs, CTLs, or Tregs (Fig. 5G-I). We observed the same trend when we expressed these populations as total cell counts (Fig. S14-S17).

To evaluate if OximUNO affected $CD206^+$ macrophages other than M2 TAMs, we analysed the state of splenic macrophages from this treatment study using FC. This analysis revealed no significant differences in the CD206/CD86 populations between the OximUNO-treated mice and PBS-treated mice (Fig. S18A-C).

While FC analysis informs on the immune status of the whole lung, it does not provide specific information regarding the TME. To characterise the immune landscape of the TME, we next analysed the expression of markers for TAMs, CTLs, and Tregs in pulmonary nodules using IF. This analysis revealed significantly lower CD206 expression in OximUNO-treated mice than PBS-treated mice (Fig. 5J, N), providing evidence for a robust reduction in the number of $CD206^+$ TAMs in the TME. Importantly, and similarly to OximUNO treatment in the orthotopic TNBC mouse model, OximUNO elicited the highest expression of CD8 (Fig. 5K, O). OximUNO and St-PGA-DOX treated mice demonstrated significantly lower lung FOXP3 expression than PBS- and DOX-treated mice (Fig. 5L, P). OximUNO-treated mice displayed between a two- and three-times higher CD8/FOXP3 expression ratio than St-PGA-DOX and DOX, and nearly seven-times higher than PBS (Fig. 5M). Therefore, our IF analysis in the pulmonary tumour nodules suggested that OximUNO triggered a shift in the immune profile of the TME towards immunostimulation.

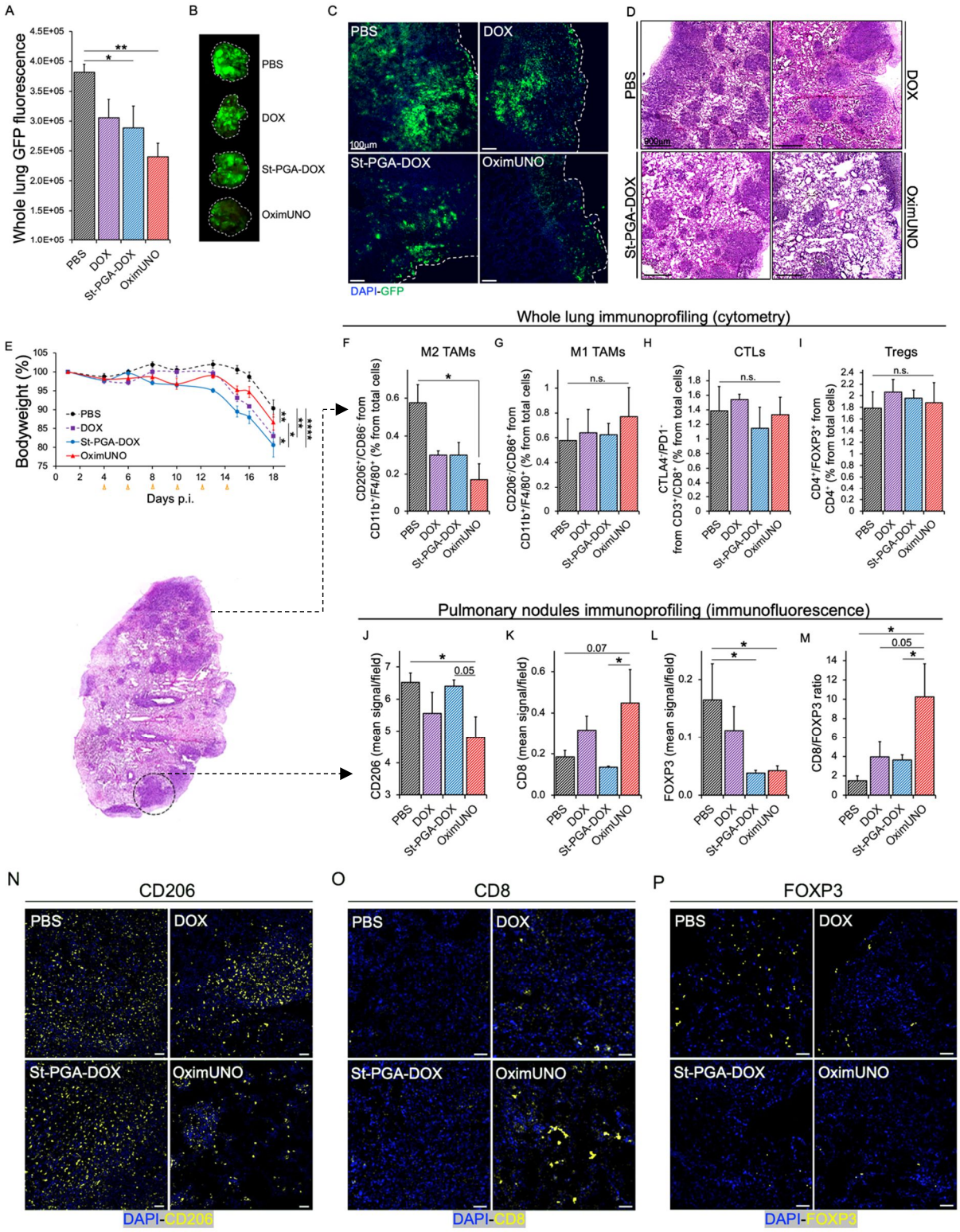

Figure 5. OximUNO treatment in experimental metastasis of TNBC significantly reduces CD206⁺ TAM number and tumour burden and alleviates immunosuppression. Treatment with OximUNO, St-PGA-DOX, or DOX at 2 mg/kg of DOX in the experimental metastasis of TNBC model, created using GFP-labelled 4T1 cells (N=6). I.p. injections began on day four p.i. and were performed every other day to give a total of six injections. (**A**) Quantification of whole lung GFP fluorescence at the experimental endpoint using the ImageJ programme (N=6). (**B**) Representative macroscopic photographs of GFP fluorescence in the lungs. (**C**) Representative

471 confocal microscopy images of GFP expression, scale bars = 100 μm. (**D**) Representative H&E images showing
472 pulmonary metastases for all groups (scale bars = 900 μm). (**E**) Mouse bodyweight analysis, demonstrating
473 significantly lower bodyweight lost with OximUNO (red line) compared with St-PGA-DOX-treated mice (blue
474 line) and DOX-treated mice (purple dotted line). Orange arrows indicate injection days. (**F-I**) FC analysis on three
475 right lungs per group. (**F**) M2 TAMs ($CD206^+$), (**G**) M1 TAMs, (**H**) CTLs and (**I**) Tregs. (**J-M**) IF analysis on the
476 pulmonary tumour nodules to detect the expression of (**J**) CD206, (**K**) CD8, and (**L**) FOXP3. (**M**) Graph showing
477 CD8/FOXP3 expression ratio. IF images quantified using the ImageJ programme from at least five images per
478 mouse and three mice per group. (**N-P**) Representative confocal microscopy images for (**N**) CD206, (**O**) CD8,
479 and (**P**) FOXP3. Scale bars = 50 μm. Error bars represent the SE of the mean.
480
481 By targeting DOX to $CD206^+$ TAMs in experimental TNBC metastases, we increased the
482 efficacy and reduced the toxicity of DOX, as OximUNO treatment associated with the presence
483 of fewer pulmonary tumour lesions and less bodyweight loss when compared to treatment with
484 untargeted St-PGA-DOX and DOX. Our results suggest that the observed therapeutic effect
485 derived from $CD206^+$ TAM depletion, which elicited an immunological shift in the TME.
486
487
488 **DISCUSSION**

489 To date, TNBC remains an aggressive breast cancer subtype[3] with few treatment options, with
490 conventional chemotherapy representing the current standard of care[20]. ICIs for TNBC have
491 provided only modest improvements in complete response and progression-free survival in a
492 small subset of TNBC patients[9,12,15,16]. Targeting TAMs can potentiate ICIs and other
493 modalities and, therefore, represents an intense area of study[57–61]; however, TAMs represent a
494 diverse population[62–64], and which TAM subtype to target remains under investigation.
495 Promising TAM-focused interventions under clinical evaluation include antibody-mediated
496 depletion of TREM2-expressing TAMs (clinical trial identifier: NCT04691375). Antibody
497 blockade of Clever-1 on M2 TAMs stimulated an M2→M1 switch in TNBC models (4T1) and
498 synergised with the PD-1 blockade[65]. Appealing studies have used anti-CD163 antibodies to
499 target TAMs[66] by decorating DOX-carrying liposomes with anti-CD163, to deplete TAMs and
500 potentiate ICIs in melanoma. Given our data comparing the tumour penetration of an anti-
501 PDL1 antibody vs. St-PGA-OG-mUNO, anti-CD163 systems may also display lower tumour
502 accumulation than St-PGA-OG-mUNO and OximUNO. Strategies targeting generic TAM
503 markers such as CSF1R and CCR2 have shown side effects and limited efficacy.

504 Motivated by the preponderance of the mannose receptor in tumourigenic/metastatic TAMs in
505 breast cancer[67–69], here, we set out to deplete CD206$^+$ TAMs in aggressive and metastatic
506 TNBC models and study the consequences on the progression and immunosuppressive state of
507 the tumour. To target CD206, a CD206-binding nanobody was developed by Ginderachter et
508 al.[70] which showed homing to CD206$^+$ TAMs in in vivo models of lung and breast cancers[70].
509 Navidea Inc. engineered a mannosylated compound[71] (Manocept™), that forms part of the
510 FDA-approved contrast agent Lymphoseek®. Unfortunately, mannose-based ligands have
511 other binding partners besides CD206, including CD209 in intestinal and genital tissues[45], and
512 can target dendritic cells[46]. Riptide Inc. also designed a peptide (RP-182) that binds to CD206;
513 however, the peptide also binds to RelB, Sirp-α and CD47[72].
514 We recently identified and described a short peptide called mUNO (sequence: CSPGAK) that
515 targets mouse[41] and human CD206[43] at a different binding site than for mannose on CD206[43].
516 We identified mUNO from an in vivo screen using a peptide library in mice bearing metastatic
517 breast cancer; we subsequently described how mUNO homed to CD206$^+$ TAMs in other solid
518 tumour models[41,73] and in early-stage models of TNBC[42] displaying low hepatic accumulation.
519 We envisioned that conjugating mUNO to St-PGA would significantly enhance targeting
520 through the avidity effect and increased plasma half-life[74].
521 Compared to synthetic polymers such as N-(2-hydroxypropyl) methacrylamide, polypeptide-
522 based nanocarriers show several benefits, including biodegradability, lower immunogenicity,
523 and a lack of long term-accumulation, and the number of polypeptide-based constructs reaching
524 clinical evaluation has significantly increased in recent years[75–77]. We employed St-PGA-based
525 nanoconjugates with three linear chains (~50 glutamic acids each) linked to a central core.
526 Overall, the safety, lack of toxicity, and biodegradability of St-PGA meet FDA approval
527 criteria[78]. A previous screen of PGA structures suggested that larger architectures enhanced
528 plasma half-life and increased bioavailability through a higher hydrodynamic volume that
529 reduces rapid renal clearance[47,79]. Of note, an extended plasma half-life will be advantageous
530 when targeting the continuously replenished TAM cell type[80,81].
531 St-PGA-OG-mUNO, a fluorescent counterpart of OximUNO, can be easily monitored by
532 immunostaining for OG or detecting native OG fluorescence (as for the half-life study). Given
533 weak DOX fluorescence and the inability to detect DOX with an antibody, we first designed
534 St-PGA-OG-mUNO for validation purposes. We then exchanged OG for DOX to generate St-
535 PGA-DOX-mUNO, referred to as "OximUNO". Our studies demonstrated that St-PGA-OG-
536 mUNO displayed a far greater plasma half-life and specificity to CD206$^+$ TAMs than free
537 mUNO and avoided CD86$^+$ M1 TAMs and CD11c$^+$ DCs, an important fact since M1 TAMs

538 display anti-tumourigenic activity[25], and CD11c$^+$ DCs participate in antigen presentation[82]. In
539 line with these observations, the computational analysis indicated that mUNO peptides are
540 available to a receptor and sweep a vast space (130°) around PGA. Altogether this data
541 demonstrates the benefit of conjugating mUNO to St-PGA. While previous studies have
542 reported the St-PGA nanocarrier[47,78] and the mUNO targeting peptide[42], this work represents
543 the first design of a peptide-targeted St-PGA nanosystem. Regarding the administration route
544 of peptide-guided St-PGA nanosystems, in the future we also wish to evaluate the i.v. route,
545 which, barring the case of intraperitoneal chemotherapy, represents a more clinically
546 translatable route to deliver cancer therapies.
547 In the OximUNO system, drug release studies revealed only 15% DOX release, which agrees
548 with our previous studies[48,50] but suggests room for improvement, which may come from using
549 longer polymer-drug linkers such as EMCH (N-ε-maleimidocaproic acid hydrazide) moiety[48,50]
550 or from the use of external triggers[83–85]. Unexpectedly, we failed to observe a significant
551 increase in DOX release in the presence of cathepsin B with respect to the hydrolytic
552 conditions; we hypothesise that the nanoconjugate conformation slows down proteolytic
553 degradation, hampering in vitro quantification within the studied timeframe[47].
554 Our in vivo efficacy studies showed that, strikingly, the sole depletion of CD206$^+$ TAMs with
555 OximUNO alleviated tumoural immunosuppression and reduced dissemination and growth,
556 confirming the pro-tumoural and immunosuppressive roles assigned to CD206$^+$ TAMs in the
557 literature and reaffirming the importance of targeting this particular TAM subset. Additionally,
558 the observed reduction in the number of CD206$^+$ TAMs and CD31$^+$ structures for OximUNO
559 agrees with the established angiogenic role of CD206$^+$ TAMs[24].
560 From a safety point of view, we found that the OximUNO nano-formulation of DOX had the
561 least negative impact on mouse bodyweight compared to free DOX or the untargeted nano-
562 formulation St-PGA-DOX. Additionally, OximUNO did not alter Crea or ALAT levels,
563 indicating the absence of acute hepatic or renal toxicity. Our data suggest that the signal
564 observed in the kidneys for St-PGA-OG-mUNO (consistent with the previously reported
565 excretion of St-PGA[47,78]) did not translate into acute renal toxicity for OximUNO. These are
566 relevant findings as DOX induces cell death and tissue damage not only in the heart but also in
567 the liver and kidneys[86]. OximUNO displayed moderate toxicity to un-polarised macrophages
568 in vitro; however, OximUNO did not affect or alter the macrophage populations of the spleen
569 in vivo, in agreement with the absence of spleen targeting we observed for St-PGA-OG-
570 mUNO.

571 Most preclinical studies evaluating the effect of M2 TAM targeted monotherapy in the 4T1
572 mouse model have either not shown efficacy on secondary tumours[87,88], a lack of efficacy in
573 primary tumours or metastases in the case of anti-CLEVER-1[65], or a pro-metastatic effect in
574 the case of anti-CSF1R[89]. Hence, along with anti-MARCO therapy[90], OximUNO constitutes
575 one of the few reports of an M2 TAM targeted monotherapy affecting both primary and
576 secondary tumours in the 4T1 mouse model.
577 Beyond TAM depletion, we show that St-PGA-mUNO represents an attractive platform to
578 carry additional therapeutic payloads other than DOX, which could include M2→M1
579 polarising agents such as TLR7 agonists[44,91], beta-emitting radiotherapeutic agents such as
580 dodecanetetraacetic acid-chelated ^{177}Lu [92], or photosensitisers used in photodynamic therapy[83–
581 85]. We also envisage the combination of TAM-depletion via OximUNO administration together
582 with current chemotherapy regimens to prevent dissemination and relapse, or the use of
583 OximUNO prior to surgery, i.e., as neoadjuvant chemotherapy
584 Taking OximUNO as a proof-of-concept, our data support the peptide-targeted St-PGA design
585 reported here as a new targeted nanosystem that could target other receptors by exchanging the
586 targeting peptide.
587
588
589 # MATERIALS AND METHODS
590 **Reagents and solutions**
591 The peptides mUNO (sequence: CSPGAK-COOH) and FAM-mUNO (FAM-Ahx-CSPGAK-
592 COOH) were purchased from TAG Copenhagen and doxorubicin (DOX) from Sigma-Aldrich.
593 St-PGA was kindly provided by Polypeptide Therapeutic Solution S.L. (PTS, Valencia, Spain).
594 See the Supplementary Information for information on all other reagents and solutions.
595 Mayer's haematoxylin solution was prepared by dissolving 5 g of aluminium potassium
596 sulphate dodecahydrate (Merck Millipore, cat. 1010421000) in 100 mL of water, and adding 1
597 g of haematoxylin (Merck, cat. H9627). After complete dissolution, 0.02 g of sodium iodide
598 (Merck, cat. 1065230100) was added and completely dissolved. Then, 2 mL of acetic acid
599 (Sigma-Aldrich, cat. 33209) was added, and then the solution was boiled and then cooled. Once
600 ready to use, the solution was filtered using a 0.45 μm filter.
601 Eosin (5%) solution was prepared by dissolving 0.5 g of Eosin Y (Sigma-Aldrich, cat. 230251)
602 in 99 mL water/1 mL acetic acid.
603

604 **Cell culture and experimental animals**

605 4T1 cells were purchased from ATCC, and 4T1-GFP cells were a gift from Ruoslahti
606 laboratory (Sanford-Burnham-Prebys Medical Discovery Institute, La Jolla, USA). 4T1 and
607 4T1-GFP cells were cultured in RPMI-1640 medium (Gibco by Life Technologies, cat. 72400-
608 021) supplemented with 10% v/v foetal bovine serum (FBS, Capricorn Scientific, cat. FBS-
609 11A) and 100 IU/mL penicillin/streptomycin (Capricorn Scientific, cat. PS-B) at 37 °C in the
610 presence of 5% CO_2. For all animal experiments, 8-12-week-old female Balb/c mice were used.
611 Animal experiment protocols were approved by the Estonian Ministry of Agriculture (Project
612 #159). All methods were performed in accordance with existing guidelines and regulations.

613

614 **Tumour models**

615 Two tumour models were used for homing studies: the orthotopic TNBC model, where $1x10^6$
616 4T1 cells in 50 µL of phosphate-buffered saline (PBS, Lonza, cat. 17-512F) were
617 subcutaneously (s.c.) injected into the fourth mammary fat pad, and the experimental metastasis
618 of TNBC model, where $5x10^5$ 4T1 cells in 100 µL of PBS were injected i.v. into Balb/c mice.
619 Two tumour models were used for treatment studies: the orthotopic TNBC model where $5x10^4$
620 4T1 cells in 50 µL of PBS were injected s.c. into fourth mammary fat pad; and the experimental
621 metastasis of TNBC model where $2x10^5$ 4T1-GFP cells in 100 µL of PBS were i.v. injected.

622

623 **Nanoconjugate synthesis and characterisation**

624 In vivo homing studies used St-PGA-OG and St-PGA-OG-mUNO, while in vitro cytotoxicity
625 and in vivo treatment studies used St-PGA-DOX and St-PGA-DOX-mUNO ("OximUNO").
626 Detailed synthetic procedures for single nanoconjugates can be found in Supplementary
627 Information.

628

629 **Physico-chemical characterisation methods**

630 <u>Nuclear magnetic resonance (NMR) spectroscopy:</u> NMR spectra were recorded at 27 °C (300
631 K) on a 300 UltrashieldTM from Bruker. Data were processed with Mestrenova software.
632 Sample solutions were prepared at the desired concentration in D_2O or D_2O supplemented with
633 $NaHCO_3$ (0.5 M).

634 <u>UV-Visible (UV-Vis) analysis:</u> UV-Vis measurements were performed using JASCO V-630
635 spectrophotometer at 25 °C with 1 cm quartz cells and a spectral bandwidth of 0.5 nm. Spectra
636 analysis was recorded three times in the range of 200–700 nm.

637 Fluorescence analysis: Fluorescence analysis was performed using a JASCO FP-6500
638 spectrofluorimeter at 25 ºC with 1 cm quartz cells.
639 Dynamic Light Scattering (DLS): Size measurements were performed using a Malvern
640 ZetasizerNano ZS instrument, supported by a 532 nm laser at a fixed scattering angle of 173°.
641 Nanoconjugate solutions (0.1 mg/mL) were freshly prepared in PBS (10 mM phosphate, 150
642 mM NaCl), filtered through a 0.45 µm cellulose membrane filter, and measured. Size
643 distribution was measured (diameter, nm) for each polymer in triplicate. Automatic
644 optimisation of beam focusing and attenuation was applied for each sample.
645 Zeta potential measurements: Zeta potential measurements were performed at 25 °C using a
646 Malvern ZetasizerNano ZS instrument, equipped with a 532 nm laser using disposable folded
647 capillary cells, provided by Malvern Instruments Ltd. Nanoconjugate solutions (0.1 mg/mL)
648 were freshly prepared in 1 mM KCl. Solutions were filtered through a 0.45 µm cellulose
649 membrane filter. Zeta potential was measured for each sample per triplicate.
650
651 **Molecular dynamics simulations**
652 Molecular dynamics (MD) simulations of PGA chains, and mUNO peptide were carried out
653 using the ff19SB force field[93] in the Amber20 MD engine[94]. The nanoconjugate system was
654 neutralised using Na+ ions and hydrated to account for a total of ~920,000 atoms (~300,000
655 TIP3P water molecules) in a truncated octahedral box. A hydrogen mass repartitioning strategy
656 was applied on the resulting topology, allowing us a 4 fs integration time step[95]. Standard
657 minimisation and equilibration protocols were used to reach 300 K and 1 atm., followed by 50
658 ns of production MD run. The simulations were run under the NVT ensemble (constant number
659 of particles, volume, and temperature through Berendsen thermostat[96]), considering periodic
660 boundary conditions. The SHAKE algorithm was used to fix hydrogen atoms[97]. The non-bound
661 cut-off value was set to Angstrom. The central moiety was parametrised using the
662 recommended protocol for the Amber force field. It was necessary to introduce amide bond,
663 angle and dihedral terms using the ParmEd module to establish the bond of the central molecule
664 to the PGA chains.
665
666 **Tumour homing studies**
667 Tumours were induced as described in the tumour model section. Tumour homing studies were
668 performed on mice bearing orthotopic TNBC or experimental metastasis of TNBC. Ten days
669 p.i. of the orthotopic TNBC or the experimental metastasis of TNBC model, mice were i.p.
670 injected with St-PGA-OG-mUNO (0.41 mg/0.5mL of PBS) or St-PGA-OG (0.35 mg/0.5mL

671 of PBS) (corresponding to 15 nmoles of OG, fluorescence measured by UV-Vis). The homing
672 of a higher dose of St-PGA-PGA-mUNO (0.82 mg/0.5mL of PBS) or St-PGA-OG (0.7
673 mg/0.5mL of PBS) (corresponding to 30 nmoles of OG) was also analysed and compared with
674 the homing of FAM-mUNO (30 nmoles/0.5mL of PBS). In every case, nanoconjugates or free
675 peptide were circulated for 6 h, after which time, mice were sacrificed by anaesthetic overdose
676 followed by cervical dislocation. Organs and tumours were collected and fixed in cold 4% w/v
677 paraformaldehyde (PFA) in PBS at +4 °C for 24 h, washed in PBS at room temperature for 1
678 h and cryoprotected in 15% w/v sucrose (Sigma Life Science, cat. S9378) followed by 30%
679 w/v sucrose at 4 °C overnight. Cryoprotected and fixed tissues were frozen in OCT (Optimal
680 Cutting Temperature, Leica, cat. 14020108926), cryosectioned at 10 µm on Superfrost+ slides
681 (Thermo Fisher, cat. J1800AMNZ) and stored at -20 °C. Immunofluorescent staining was
682 performed as described earlier[42]. OG was detected using rabbit anti-FITC/Oregon Green
683 (dilution 1/100, Invitrogen by Thermo Fisher Scientific, cat. A889) and Alexa Fluor® 647 goat
684 anti-rabbit antibody (dilution 1/250, Invitrogen by Thermo Fisher Scientific, cat. A21245).
685 CD206 was detected using rat anti-mouse CD206 (dilution 1/150, Bio-Rad, cat. MCA2235GA)
686 and Alexa Fluor® 546 goat anti-rat antibody (dilution 1/250, life technologies, cat. A11081).
687 CD86 was detected using rat anti-mouse CD86 (dilution 1/100, BioLegend, cat. 105001) and
688 Alexa Fluor® 546 goat anti-rat secondary antibody (dilution 1/250). CD11c was detected using
689 hamster anti-mouse CD11c antibody (dilution 1/75, BioLegend, cat. 117301) and Alexa
690 Fluor® 546 goat anti-hamster secondary antibody (dilution 1/200, life technologies, cat.
691 A21111) Slides were counterstained using 4′,6-diamidino-2-phenylindole (DAPI, 1 µg/mL in
692 PBS, Sigma-Aldrich, cat. D9542-5MG). Coverslips were mounted using mounting medium
693 (Fluoromount-G™ Electron Microscopy Sciences, cat. 17984-25), and sections were imaged
694 using Zeiss confocal microscope (Zeiss LSM-710) and 20x objective. The colocalisation
695 analysis shown in Fig. 2M-P, between the FAM or OG channel and the CD206 channel was
696 carried out using the "Coloc2" plugin in the Fiji programme and selecting the "Pearson's R
697 value (no threshold)" coefficient. The colocalisation values were obtained from at least three
698 representative images per mouse per group and their average and standard error were plotted.
699 The OG/FAM mean signal per $CD206^+$ cell analysis was measured using the ImageJ
700 programme, taking the mean OG/FAM signal, and dividing it with the number of $CD206^+$ cells.
701 Average values were obtained from four images per mouse. N=3 for orthotopic TNBC and
702 N=2 for the homing in experimental metastasis of TNBC.
703

704 **Analysis of tumour and liver leakiness**

705 Endogenous IgG immunostaining of orthotopic 4T1 tumours and livers was performed
706 following the same IF protocol as described above to assess leakiness. Endogenous IgG was
707 detected using Alexa Fluor® 647 goat anti-mouse antibody (dilution 1/200, Invitrogen by
708 Thermo Fisher Scientific, cat. A21235) and slides were counterstained with DAPI (1 µg/mL in
709 PBS). The coverslips were mounted, and sections were imaged using Zeiss confocal
710 microscope and 20x objective (N=3 tumours).

711

712 **PDL1 expression analysis in orthotopic TNBC tumours**

713 The assessment of PDL1 expression in orthotopic 4T1 tumours followed the IF protocol
714 described above. PDL1 was detected using rat anti-mouse PDL1 (dilution 1/100, BioLegend,
715 cat. 124302) as primary antibody and Alexa Fluor® 647 goat anti-rat (dilution 1/200,
716 Invitrogen, cat. A21247) as the secondary antibody. Slides were counterstained with DAPI (1
717 µg/mL in PBS), mounted, and imaged using a Zeiss confocal microscope.

718

719 **Tumour homing of anti-PDL1 in orthotopic TNBC tumours**

720 For the homing analysis with anti-PDL1, we injected $1x10^6$ 4T1 cells in 50 µL of PBS s.c. and
721 ten days p.i., PDL1 antibody (5 mg/kg, rat anti-mouse, BioXcell, cat. BE0101) was injected
722 i.v., circulated for 24 h after which time, mice were sacrificed, organs collected and fixed with
723 PFA. Ten µm tissue sections were stained with Alexa Fluor® 647 goat anti-rat antibody
724 (dilution 1/200), counterstained with DAPI (1 µg/mL in PBS), mounted, and imaged with a
725 Zeiss confocal microscope.

726

727 **Plasma half-life evaluation for St-PGA-OG-mUNO**

728 Plasma half-life studies were performed as previously described[42]. Briefly, healthy female
729 Balb/c mice (N=3) were i.p. injected with St-PGA-OG-mUNO (0.41 mg/0.5mL of PBS,
730 corresponding to 15 nmoles OG). Ten µL of blood was sampled at different timepoints (0, 5,
731 10, 15, 30, 60, 180, 360, and 1440 min) and mixed with 50 µL of PBS-Heparin solution. Blood
732 samples were centrifuged to obtain plasma (300g for 5 min at room temperature) and OG
733 fluorescence was read with a plate reader (FlexStation II Molecular Devices) at 480nm
734 excitation/520nm emission.

735

736

737 **DOX release studies**

738 LC-MS was implemented to determine free drug levels, stability, and drug release with
739 OximUNO. The LC-MS system consisted of an ExionLC LC system and AB Sciex QTRAP
740 4500, a triple quadrupole ion trap hybrid equipped with a Turbo VTM electrospray ionisation
741 source. DOX was detected with an internal standard method: 1 µg/mL of daunorubicin (DAU)
742 was used as internal standard, where three calibration curves (in a range from 0.5 to 50 µg/mL
743 DOX) were prepared and used for accurate analysis of DOX in the samples. Both DOX and
744 DAU were detected with positive electrospray ionisation mode by following two mass
745 transitions (544.2 m/z → 397 m/z and 544.2 m/z → 379 m/z for DOX, and 528 m/z → 363.1
746 m/z and 528 m/z → 321.3 m/z for DAU). The obtained LC-MS optimal conditions were as
747 follows: flow rate 0.5 mL/min; mobile phase – 0.05 % trifluoroacetic acid with 70 % of
748 acetonitrile; LiChrospher 100 C18 column (125x4.0 mm) (Merck); column temperature 40 ºC,
749 10 µL injection volume.

750 Stability study of OximUNO conjugate in PBS, pH 7.4

751 OximUNO was incubated in 10 mM dPBS at 37 °C at the concentration of 3 mg/mL and with
752 3 µg/mL of DAU. 100 µL aliquots were collected at defined time points (0, 1, 2, 5, 24, 48, 72
753 h), extracted with 3x250 µL chloroform, and mixed by vortexing for 5 min. Organic phases
754 from all three chloroform extracts were collected in one tube, evaporated using speed vacuum,
755 and stored at -20 °C. On the day of analysis, dried samples were reconstituted in 300 µL of
756 methanol (LC-MS grade), vortexed for 5 min and centrifuged for 5 min at 30,437g.
757 Supernatants were filtered through a 0.45 µm filter and subjected to LC-MS analysis.

758 Stability study of OximUNO in the i.p. fluid

759 I.p. fluid was collected from healthy 8-12-week old Balb/c female mice as performed in REF[98]
760 by collecting the supernatant and discarding the pellet after the centrifugation step. A working
761 solution containing 3 mg/mL of OximUNO and 3 µg/mL of DAU in i.p. fluid was incubated
762 at 37 °C. 50 µL aliquots were collected at scheduled time points (0, 2, 5, 7, and 24 h). Samples
763 were then diluted with 100 µL of methanol, sonicated to dissolve DOX, and injected into the
764 LC-MS after filtration through a 0.45 µm filter.

765 Cathepsin B release kinetic studies.

766 Cathepsin B (5 IU) was activated in 2 mM EDTA, 5 mM DTT, and 20 mM CH_3COONa buffer
767 and incubated at 37 °C for 15 min. In a separate tube, a solution containing 3 mg/mL OximUNO
768 and 3 µg/mL of DAU was prepared with 20 mM CH_3COONa and incubated at 37 °C for 15
769 min. The two solutions were then combined to produce a reaction solution that was incubated
770 at 37 °C. 100 µL aliquots were collected at scheduled time points (0, 1, 2, 5, 8, 24, 48, 72 h),

771 and after the addition of 900 µL of dPBS (to adjust the pH level to 7.4), free DOX and DAU
772 were extracted with 2.5 mL of $CHCl_3$ three times. Samples were processed as described under
773 "Stability Study of OximUNO conjugate in PBS, pH 7.4". After $CHCl_3$ evaporation, samples
774 were reconstituted with 300 µL of methanol, filtered through a 0.45 µm filter and subjected to
775 LC-MS analysis. A blank solution was prepared with the same components as the sample
776 solution but without cathepsin B and used as a control sample.
777
778 **In vitro cytotoxicity assay**
779 Human peripheral blood mononuclear cells (PBMC) were purified from human blood buffy
780 coat using Ficoll Paque Plus (GE Healthcare, cat. 17-1440-02) reagent and $CD14^+$ microbeads
781 (MACS Miltenyi Biotec, cat. 130-050-201) as previously described[42]. $1.2x10^5$ cells in 50 µL
782 of RPMI-1640 medium were seeded on an FBS-coated 96-well plate. To obtain M0
783 macrophages, 50 µL of macrophage colony stimulating factor (M-CSF) (100 ng/mL,
784 BioLegend, cat. 574802) was added and replenished every other day for four days by
785 substituting the half of the medium with fresh medium containing M-CSF. To obtain optimal
786 macrophage attachment and M2 polarisation, 50 µL of interleukin-4 (IL-4, 50 ng/mL,
787 BioLegend, cat. 574002) and M-CSF (100 ng/mL) mixture was added to the wells. The medium
788 was replenished by substituting half of the medium with fresh medium containing IL-4 and M-
789 CSF every other day for six days. To obtain M1 macrophages, monocytes were incubated with
790 M-CSF (100 ng/mL) for six days, replenishing every other day with fresh medium containing
791 M-CSF and on day six, 50 µL of M-CSF, lipopolysaccharide (LPS, 100 ng/mL, Sigma Aldrich,
792 cat. L4391) and interferon-γ (IFN-γ, 20 ng/mL, BioLegend, cat. 570202) was added and
793 incubated overnight. On day seven for M2 and M1 macrophages or day four for M0
794 macrophages, cells were incubated for 15 min at 37 °C with OximUNO, St-PGA-DOX, DOX
795 in medium, or free medium as a control (N=3 wells per group). Concentrations used were
796 calculated based on DOX: 33µM and 100µM. (Of note, the dose of OximUNO used for the 33
797 µM DOX experiments shown in Figure 3E corresponds to the same dose of OximUNO used
798 for both in vivo treatment studies. In vivo, all treated groups received injections containing 2
799 mg/kg of DOX, which, assuming the dilution in mouse blood, corresponds to a DOX
800 concentration of 33 µM). After incubation, wells were washed, fresh medium added, and cells
801 incubated for 48 h at 37 °C. After 48 h, 10 µL of 3-(4,5-dimethylthiazol-2-yl)-2,5-
802 diphenyltetrazolium bromide (MTT, concentration 5 mg/mL, Invitrogen, cat. M6494) in PBS
803 was added to each well containing culture medium and incubated for 2.5 h at 37 °C. Medium

804 containing MTT was then removed without removing formed crystals, and 100 μL of
805 isopropanol was added to each well to dissolve crystals. Absorbance was read at 580 nm using
806 a plate reader (Tecan Sunrise) and the corresponding Magellan™ 7 programme.
807
808 **In vivo liver and kidney toxicology studies with OximUNO**
809 Three healthy 12-week-old female Balb/c mice were i.p. injected once with OximUNO (0.704
810 mg/0.5mL PBS or 1.408mg/0.5mL) and circulated for 48 h. Then, mice were anesthetised, and
811 blood collected through retro-orbital bleeding into Lithium Heparin tubes (BD Vacutainer, cat.
812 368494). Blood samples were centrifuged at 1800g for 15 min at +4 °C and 400 μL of plasma
813 was collected for analysis. Samples were analysed in Tartu University Hospital using a Cobas
814 6000 IT-MW (Roche Diagnostics Gmbh) machine and reagents for creatinine (CREP2, cat.
815 03263991) and alanine aminotransferase (ALTLP, cat. 04467388).
816
817 **OximUNO treatment of orthotopic TNBC**
818 $5x10^4$ 4T1 cells in 50 μL of PBS were s.c. injected into the fourth mammary fat pad of 8-12-
819 week-old female Balb/c mice. On day seven, mice were sorted into four groups by tumour
820 volume measured using a digital calliper (Mitutoyo). Tumour volume was calculated based on
821 the formula $(W^2 \times L)/2$, where W is the tumour's width and L is the tumour's length. The
822 starting volume for each group was ~25 mm^3, and the number of mice in each group was five.
823 The first i.p. injection of compounds was carried out on day seven, followed by an i.p. injection
824 every other day; nine injections were performed in total. The dose of nanoconjugates was
825 calculated based on DOX, 2 mg/kg per injection (DOX: 39.5 μg/0.5mL PBS; St-PGA-DOX:
826 476 μg/0.5mL PBS; OximUNO: 341 μg/0.5mL PBS) giving a cumulative dose of DOX of 18
827 mg/kg. Mouse bodyweight and tumour volumes were monitored every other day. The final
828 injection was on day 25 and all mice were sacrificed on day 28. Tumour tissues were processed
829 as described under "In vivo biodistribution studies", and the lungs and hearts were embedded
830 in paraffin and processed for haematoxylin and eosin (H&E) staining (described below).
831 Tumours were immunostained as described above. CD206 was detected using rat anti-mouse
832 CD206 (dilution 1/200), CD8 using rat anti-mouse CD8 (dilution 1/75 Biolegend, cat. number
833 100701), FOXP3 using rat anti-mouse FOXP3 (dilution 1/75, Biolegend, cat number 126401)
834 as primary antibodies, Alexa Fluor® goat anti-rat 647 (dilution 1/300 for CD206 and 1/200 for
835 CD8, FOXP3,) was used as a secondary antibody for all markers. Slides were counterstained
836 with DAPI (1 μg/mL in PBS) and imaged using a Zeiss confocal microscope with a 10x

837 objective. All five tumours from each group were included in the IF analysis and at least three
838 images per mouse per group were included. Fluorescent signal intensity was calculated using
839 the ImageJ programme; to account for different amounts of tissue in the different images, only
840 the area containing tissue was selected and the "mean signal intensity" given by the programme
841 taken (total integrated intensity divided by the selected area). For this analysis, at least three
842 images per tumour were included.
843
844 **H&E staining in paraffin-embedded formalin-fixed tissues**
845 For H&E staining, 2 μm sections were cut from paraffin-embedded blocks. Slides were
846 warmed at 60 °C for 2 min before deparaffinising using xylene (3x2 min, 1x1 min) followed
847 by 100% ethanol washes (3x1 min), 80% ethanol wash (1x1 min) followed by 1 min wash in
848 water. Slides were first incubated with ST-1 HemaLast for 30 s, followed by ST-2
849 Haematoxylin for 5 min after which time, slides were washed in water for 2 min. Then, ST-3
850 Differentiator was added for 45 s, and slides were washed in water for 1 min. Next, ST-4 Bluing
851 Agent was added (1 min), washed for 1 min in water followed by 1 min incubation in 80%
852 ethanol, after which time, ST-5 Eosin was added and incubated for 1 min. For rehydration,
853 incubations in 100% ethanol (2x30 s, 1x2 min) were carried out and finished with incubations
854 in xylene (2x2 min). All washes were carried out in tap water. H&E stainings were performed
855 in Tartu University Hospital by pathologists using Leica staining automat and ST Infinity H&E
856 Staining System (Leica, cat. 38016998). Stained lung sections were scanned using a slide
857 scanner (Leica SCN400) and 20x zoom. Images were analysed using the QuPath programme
858 (version 0.1.2)[99]. Five levels ~1 mm apart were used for each mouse to obtain comprehensive
859 pulmonary metastases profile. Stained heart sections were also scanned using a slide scanner
860 and analysed with the QuPath programme. Tartu University Hospital pathologists assessed
861 cardiotoxicity in hearts and pulmonary metastases.
862
863 **Analysis of CD31 expression and blood vessel count**
864 CD31 expression after treating orthotopic TNBC tumours with OximUNO, St-PGA-DOX, or
865 DOX was detected using rat anti-mouse CD31 (dilution 1/100, BD Biosciences, cat. 553370)
866 and Alexa Fluor® 546 goat anti-rat (dilution 1/200, Invitrogen, cat. A11081) was used as the
867 secondary antibody. Slides were counterstained with DAPI (1 μg/mL in PBS) and imaged using
868 Zeiss confocal microscope with a 10x objective. CD31 expression was calculated using ImageJ
869 and mean signal per field as described under "OximUNO therapy in orthotopic TNBC",

870 including at least five images per mouse per group, N=5 mice per group. The blood vessel
871 count was calculated from the same images using ImageJ as follows: the image was changed
872 to an 8-bit image, threshold (Triangle algorithm with modifications to account for as much
873 actual CD31 signal as possible) was added, and particles analysed. At least three images per
874 mouse per group were included in the analysis, N=5 mice per group. Field size was 1.42 mm
875 x 1.42 mm for all images.
876
877 **OximUNO treatment of experimental metastasis of TNBC**
878 $2x10^5$ 4T1 cells in 100 µL of PBS were i.v. injected into the tail vein of 8-12-week-old female
879 Balb/c mice. Treatment with OximUNO, St-PGA-DOX, or DOX began on day four p.i.; each
880 group comprised six mice. Doses of different compounds were calculated based on DOX (2
881 mg/kg): DOX: 39.5 µg/0.5mL PBS; St-PGA-DOX: 774.5 µg/0.5mL PBS; OximUNO: 704
882 µg/0.5mL PBS. Mouse bodyweight was monitored every other day. A total of six injections
883 were carried out every other day. The final injection was on day 12, and all animals were
884 sacrificed on day 18 using anaesthetic overdose and perfusion with PBS. Three right lungs
885 from each group were analysed with flow cytometry (FC), and three full lungs and three left
886 lungs from each group were frozen into blocks using OCT. Frozen lung tissues were
887 cryosectioned as described earlier, fixed with cold 4% PFA (CD206) or acetone (for CD8 and
888 FOXP3), and stained as described in the following section. Immunofluorescent stainings were
889 performed using the same markers and antibodies as shown in the "OximUNO treatment in
890 orthotopic TNBC" section.
891
892 **GFP staining and imaging**
893 Six lungs from each group were frozen in OCT. Ten µm sections were cut, and slides were
894 kept at -20 °C until ready to use. Slides were taken out of the freezer at least 30 min before
895 staining. For staining, slides were fixed with 4% PFA for 10 min at room temperature, washed
896 with PBS for 10 min at room temperature, counterstained using DAPI (1 µg/mL in PBS) for 5
897 min at room temperature, washed 3x4 min with PBS and finally mounted using mounting
898 medium. Permeabilisation was not used in this step to improve GFP visualisation. GFP was
899 visualised using its native fluorescence. Slides were imaged using Olympus confocal
900 microscope (FV1200MPE) with a 10x objective.
901
902

903 **Macroscopic analysis of GFP Signal**

904 Lungs from each group were imaged using Illumatool Bright Light System LT-9900
905 (LightTool's Research) in the green channel to visualise the fluorescent signal
906 macroscopically, and a photograph of each lung was taken. The total GFP signal of each lung
907 was quantified using the ImageJ programme using the "IntDen" value.

908

909 **Flow cytometry analysis**

910 Three mice were sacrificed using anaesthetic overdose, perfused with PBS and right lung
911 tissues were placed in cold RPMI-1640 medium supplemented with 2% v/v FBS. Lungs were
912 cut into small pieces on ice in a solution containing collagenase IV (160 U/mL, Gibco
913 cat.17104019)/dispase (0.6 U/mL, Gibco, cat. 17105-041)/DNase I (15 U/mL; AppliChem, cat.
914 A3778) mixture. To obtain a single-cell suspension, lung pieces were incubated in 10 mL of
915 the same mixture at 37 °C on a rotating platform for 45-60 min, pipetting every 10 min to
916 improve digestion. The cells were washed with 5 mL of RB ("running buffer": 4 mL 0.5M
917 EDTA, 100 mL v/v FBS in 1L of PBS), centrifuged (350g, 7 min, 4 °C), and red blood cells
918 were lysed with 3 mL of ammonium-chloride-potassium lysing buffer (ACK) at room
919 temperature. Ten mL of RB was added, cells were centrifuged and filtered using a 100 µm cell
920 strainer (Falcon, cat. 352360). Cells were counted using the brightfield mode of LUNA™
921 Automated Cell counter (Logos Biosystems). Cells were collected in RB at a concentration of
922 $5x10^6$/100µL, placed on a 96-well plate with conical bottom and incubated for 30 min in FcR-
923 blocking 2.4G2 hybridoma medium at 4 °C. The cells were then stained for either macrophage
924 or T cell markers for 25-45 min in the dark at +4 °C, centrifuged and washed twice with RB.
925 The antibodies used are listed in Table 2. For intracellular staining of T cells, cells were fixed
926 using eBioscience™ FOXP3/Transcription Factor Staining Buffer Set (Thermo Fisher, cat. 00-
927 5523-00) according to the protocol provided. Cells were stained for 25-45 min in the dark at
928 room temperature following permeabilisation and washed twice using RB. All cells were
929 collected in 150 µL of RB, filtered through a 70 µm filter (Share Group Limited) and 150 µL
930 of RB was used to wash the filter. BD LSRFortessa Flow Cytometer and FCS Express 7 Flow
931 (De Novo Software) were used for analysis.

932

933

934

935

936 **Table 2. Antibodies used in FC analysis: macrophage and T cell markers.**

	Antibody	Dilution, company
Macrophage markers	PerCP/Cyanine5.5 anti-mouse CD206 (MMR)	1/200, BioLegend, clone C068C2, cat. 141715
	PE anti-mouse CD86	1/400, BioLegend, clone PO3, cat. 105105
	PE/Cyanine7 anti-mouse F4/80	1/200, BioLegend, clone BM8, cat. 123114
	PE/Dazzle™ 594 anti-mouse/human CD11b	1/ 800, BioLegend, clone M1/70, cat. 101255
	eBioscience™ Fixable Viability Due eFluor™ 506	1/800, Thermo Fisher Scientific, cat. 65-0866-18
T cell markers	Brilliant Violet 570™ anti-mouse CD4	1/400, BioLegend, clone RM4-5, cat. 100542
	Brilliant Violet 605™ anti-mouse CD8a	1/400, BioLegend, clone 53-6.7, cat. 100744
	PE/Dazzle™ 594 anti-mouse CD279 (PD-1)	1/200, BioLegend, clone 29F.1A12, cat. 135228
	Alexa Fluor® 488 anti-mouse FOXP3	1/100, BioLegend, clone MF-14, cat 126406
	PerCP/Cyanine5.5 anti-mouse CD3ε	1/200, BioLegend, clone 145-2C11, cat. 100328
	Brilliant Violet 421™ anti-mouse CD152 (CTLA4)	1/200, BioLegend, clone UC10-4B9, cat. 106312
	eBioscience™ Fixable Viability Due eFluor™ 506	1/800, Thermo Fisher Scientific, cat. 65-0866-18

937

938 **H&E staining on PFA-fixed cryosections**

939 Ten µm sections were cut from unfixed tissues in a frozen block; sections were stored at -20
940 °C until ready to use. When ready, slides were taken out of the freezer at least 30 min before
941 staining. Room temperature slides were fixed with cold 4% PFA for 10 min at room
942 temperature followed by washing in PBS for 10 min at room temperature. After washing, slides
943 were dipped into Mayer's haematoxylin solution (see preparation under "Reagents and
944 Solutions") for 10 s, followed by washing in running tap water for 5 min. Then, slides were
945 dipped into Eosin (5%) solution (see preparation under "Reagents and Solutions") for 20 s,
946 followed by washing in running tap water for 5 min. For rehydration, slides were placed first
947 in 96% ethanol (2x2min) followed by 100% ethanol (2x2min). For clearance slides were placed
948 in RotiClear® solution (Roth, cat. A538.5) for two-times 5 min, after which time, slides were
949 mounted using Eukitt® quick-hardening mounting medium (Merck, cat. 03989). Slides were
950 scanned using Leica DM6 B microscope and Leica Aperio Versa 8 slides scanner with 20x
951 zoom and images were analysed using the ImageScope programme (version 12.3.3).

952

953 **Statistical analysis**

954 All statistical analysis was carried out using One-Way ANOVA and Fisher LSD tests, using
955 the Statistica programme (release 7).

956

957 **DATA AVAILABILITY**

958 All data needed to evaluate the conclusions on the paper are presented in the paper and/or the
959 Supplementary Information. Additional data related to the findings of this study are available
960 from the corresponding authors.

961

962

963 # REFERENCES

964 1. Rivenbark, A. G., O'Connor, S. M. & Coleman, W. B. Molecular and cellular
965 heterogeneity in breast cancer: challenges for personalized medicine. *Am. J. Pathol.* **183**,
966 1113–1124 (2013).
967 2. Foulkes, W. D., Smith, I. E. & Reis-Filho, J. S. Triple-Negative Breast Cancer. *N. Engl. J.*
968 *Med.* **363**, 1938–1948 (2010).
969 3. Lehmann, B. D. *et al.* Identification of human triple-negative breast cancer subtypes and
970 preclinical models for selection of targeted therapies. *J. Clin. Invest.* **121**, 2750–2767
971 (2011).
972 4. Garrido-Castro, A. C., Lin, N. U. & Polyak, K. Insights into Molecular Classifications of
973 Triple-Negative Breast Cancer: Improving Patient Selection for Treatment. *Cancer*
974 *Discov.* **9**, 176–198 (2019).
975 5. Pardoll, D. M. The blockade of immune checkpoints in cancer immunotherapy. *Nat. Rev.*
976 *Cancer* **12**, 252–264 (2012).
977 6. Esfahani, K. *et al.* A Review of Cancer Immunotherapy: From the Past, to the Present, to
978 the Future. *Curr. Oncol.* **27**, 87–97 (2020).
979 7. Adams, S. *et al.* Current Landscape of Immunotherapy in Breast Cancer: A Review. *JAMA*
980 *Oncol.* **5**, 1205–1214 (2019).
981 8. Gong, J., Chehrazi-Raffle, A., Reddi, S. & Salgia, R. Development of PD-1 and PD-L1
982 inhibitors as a form of cancer immunotherapy: a comprehensive review of registration
983 trials and future considerations. *J. Immunother. Cancer* **6**, 8 (2018).

984 9. Schmid, P. *et al.* Atezolizumab and Nab-Paclitaxel in Advanced Triple-Negative Breast
985 Cancer. *N. Engl. J. Med.* **379**, 2108–2121 (2018).
986 10. Schmid, P. *et al.* Atezolizumab plus nab-paclitaxel as first-line treatment for
987 unresectable, locally advanced or metastatic triple-negative breast cancer (IMpassion130):
988 updated efficacy results from a randomised, double-blind, placebo-controlled, phase 3
989 trial. *Lancet Oncol.* **21**, 44–59 (2020).
990 11. Marra, A., Viale, G. & Curigliano, G. Recent advances in triple negative breast
991 cancer: the immunotherapy era. *BMC Med.* **17**, 90 (2019).
992 12. Mori, H. *et al.* The combination of PD-L1 expression and decreased tumor-infiltrating
993 lymphocytes is associated with a poor prognosis in triple-negative breast cancer.
994 *Oncotarget* **8**, 15584–15592 (2017).
995 13. Mittendorf, E. A. *et al.* PD-L1 Expression in Triple-Negative Breast Cancer. *Cancer*
996 *Immunol. Res.* **2**, 361–370 (2014).
997 14. Socinski, M. A. *et al.* Atezolizumab for First-Line Treatment of Metastatic
998 Nonsquamous NSCLC. *N. Engl. J. Med.* **378**, 2288–2301 (2018).
999 15. Adams, S. *et al.* Patient-reported outcomes from the phase III IMpassion130 trial of
1000 atezolizumab plus nab-paclitaxel in metastatic triple-negative breast cancer. *Ann. Oncol.*
1001 **31**, 582–589 (2020).
1002 16. Fecher, L. A., Agarwala, S. S., Hodi, F. S. & Weber, J. S. Ipilimumab and Its
1003 Toxicities: A Multidisciplinary Approach. *The Oncologist* **18**, 733–743 (2013).
1004 17. Hunter, G., Voll, C. & Robinson, C. A. Autoimmune inflammatory myopathy after
1005 treatment with ipilimumab. *Can. J. Neurol. Sci. J. Can. Sci. Neurol.* **36**, 518–520 (2009).
1006 18. Maker, A. V. *et al.* Tumor Regression and Autoimmunity in Patients Treated With
1007 Cytotoxic T Lymphocyte–Associated Antigen 4 Blockade and Interleukin 2: A Phase I/II
1008 Study. *Ann. Surg. Oncol.* **12**, 1005–1016 (2005).

1009 19. Phan, G. Q. *et al.* Cancer regression and autoimmunity induced by cytotoxic T
1010 lymphocyte-associated antigen 4 blockade in patients with metastatic melanoma. *Proc.*
1011 *Natl. Acad. Sci. U. S. A.* **100**, 8372–8377 (2003).
1012 20. Cretella, D. *et al.* Pre-treatment with the CDK4/6 inhibitor palbociclib improves the
1013 efficacy of paclitaxel in TNBC cells. *Sci. Rep.* **9**, 13014 (2019).
1014 21. Arola, O. J. *et al.* Acute Doxorubicin Cardiotoxicity Involves Cardiomyocyte
1015 Apoptosis. *Cancer Res.* **60**, 1789–1792 (2000).
1016 22. Zhang, S. *et al.* Identification of the molecular basis of doxorubicin-induced
1017 cardiotoxicity. *Nat. Med.* **18**, 1639–1642 (2012).
1018 23. Keklikoglou, I. *et al.* Chemotherapy elicits pro-metastatic extracellular vesicles in
1019 breast cancer models. *Nat. Cell Biol.* **21**, 190–202 (2019).
1020 24. Hughes, R. *et al.* Perivascular M2 Macrophages Stimulate Tumor Relapse after
1021 Chemotherapy. *Cancer Res.* **75**, 3479–3491 (2015).
1022 25. Lewis, C. E. & Pollard, J. W. Distinct Role of Macrophages in Different Tumor
1023 Microenvironments. *Cancer Res.* **66**, 605–612 (2006).
1024 26. Peranzoni, E. *et al.* Macrophages impede CD8 T cells from reaching tumor cells and
1025 limit the efficacy of anti–PD-1 treatment. *Proc. Natl. Acad. Sci.* **115**, E4041–E4050
1026 (2018).
1027 27. Neubert, N. J. *et al.* T cell–induced CSF1 promotes melanoma resistance to PD1
1028 blockade. *Sci. Transl. Med.* **10**, eaan3311 (2018).
1029 28. Daurkin, I. *et al.* Tumor-Associated Macrophages Mediate Immunosuppression in the
1030 Renal Cancer Microenvironment by Activating the 15-Lipoxygenase-2 Pathway. *Cancer*
1031 *Res.* **71**, 6400–6409 (2011).

1032 29. Gok Yavuz, B. *et al.* Cancer associated fibroblasts sculpt tumour microenvironment
1033 by recruiting monocytes and inducing immunosuppressive PD-1+ TAMs. *Sci. Rep.* **9**, 3172
1034 (2019).
1035 30. Pathria, P., Louis, T. L. & Varner, J. A. Targeting Tumor-Associated Macrophages in
1036 Cancer. *Trends Immunol.* **40**, 310–327 (2019).
1037 31. DeNardo, D. G. *et al.* Leukocyte Complexity Predicts Breast Cancer Survival and
1038 Functionally Regulates Response to Chemotherapy. *Cancer Discov.* **1**, 54–67 (2011).
1039 32. Mancini, V. S. B. W., Pasquini, J. M., Correale, J. D. & Pasquini, L. A. Microglial
1040 modulation through colony-stimulating factor-1 receptor inhibition attenuates
1041 demyelination. *Glia* **67**, 291–308 (2019).
1042 33. Lee, S., Shi, X. Q., Fan, A., West, B. & Zhang, J. Targeting macrophage and
1043 microglia activation with colony stimulating factor 1 receptor inhibitor is an effective
1044 strategy to treat injury-triggered neuropathic pain. *Mol. Pain* **14**, 1744806918764979
1045 (2018).
1046 34. Bissinger, S. *et al.* Macrophage depletion induces edema through release of matrix-
1047 degrading proteases and proteoglycan deposition. *Sci. Transl. Med.* **13**, eabd4550 (2021).
1048 35. Wesolowski, R. *et al.* Phase Ib study of the combination of pexidartinib (PLX3397), a
1049 CSF-1R inhibitor, and paclitaxel in patients with advanced solid tumors. *Ther. Adv. Med.*
1050 *Oncol.* **11**, 1758835919854238 (2019).
1051 36. Papadopoulos, K. P. *et al.* First-in-Human Study of AMG 820, a Monoclonal Anti-
1052 Colony-Stimulating Factor 1 Receptor Antibody, in Patients with Advanced Solid Tumors.
1053 *Clin. Cancer Res.* **23**, 5703–5710 (2017).
1054 37. Kitamura, T. *et al.* Monocytes Differentiate to Immune Suppressive Precursors of
1055 Metastasis-Associated Macrophages in Mouse Models of Metastatic Breast Cancer. *Front.*
1056 *Immunol.* **8**, (2018).

1057 38. Madsen, D. H. *et al.* Tumor-Associated Macrophages Derived from Circulating
1058 Inflammatory Monocytes Degrade Collagen through Cellular Uptake. *Cell Rep.* **21**, 3662–
1059 3671 (2017).
1060 39. Ishihara, D. *et al.* Wiskott-Aldrich Syndrome Protein Regulates Leukocyte-Dependent
1061 Breast Cancer Metastasis. *Cell Rep.* **4**, 429–436 (2013).
1062 40. Karousou, E. *et al.* Collagen VI and Hyaluronan: The Common Role in Breast
1063 Cancer. *BioMed Res. Int.* **2014**, 1–10 (2014).
1064 41. Scodeller, P. *et al.* Precision Targeting of Tumor Macrophages with a CD206 Binding
1065 Peptide. *Sci. Rep.* **7**, 14655 (2017).
1066 42. Lepland, A. *et al.* Targeting Pro-Tumoral Macrophages in Early Primary and
1067 Metastatic Breast Tumors with the CD206-Binding mUNO Peptide. *Mol. Pharm.* **17**,
1068 2518–2531 (2020).
1069 43. Asciutto, E. K. *et al.* Phage-Display-Derived Peptide Binds to Human CD206 and
1070 Modeling Reveals a New Binding Site on the Receptor. *J. Phys. Chem. B* **123**, 1973–1982
1071 (2019).
1072 44. Figueiredo, P. *et al.* Peptide-guided resiquimod-loaded lignin nanoparticles convert
1073 tumor-associated macrophages from M2 to M1 phenotype for enhanced chemotherapy.
1074 *Acta Biomater.* **133**, 231–243 (2021).
1075 45. Jameson, B. *et al.* Expression of DC-SIGN by Dendritic Cells of Intestinal and
1076 Genital Mucosae in Humans and Rhesus Macaques. *J. Virol.* **76**, 1866–1875 (2002).
1077 46. Conniot, J. *et al.* Immunization with mannosylated nanovaccines and inhibition of the
1078 immune-suppressing microenvironment sensitizes melanoma to immune checkpoint
1079 modulators. *Nat. Nanotechnol.* **14**, 891–901 (2019).

1080 47. Duro-Castano, A. *et al.* Well-Defined Star-Shaped Polyglutamates with Improved
1081 Pharmacokinetic Profiles As Excellent Candidates for Biomedical Applications. *Mol.*
1082 *Pharm.* **12**, 3639–3649 (2015).
1083 48. Arroyo-Crespo, J. J. *et al.* Tumor microenvironment-targeted poly-L-glutamic acid-
1084 based combination conjugate for enhanced triple negative breast cancer treatment.
1085 *Biomaterials* **186**, 8–21 (2018).
1086 49. Duro-Castano, A. *et al.* Polyglutamic acid-based crosslinked doxorubicin nanogels as
1087 an anti-metastatic treatment for triple negative breast cancer. *J. Controlled Release* **332**,
1088 10–20 (2021).
1089 50. Arroyo-Crespo, J. J. *et al.* Anticancer Activity Driven by Drug Linker Modification in
1090 a Polyglutamic Acid-Based Combination-Drug Conjugate. *Adv. Funct. Mater.* **28**,
1091 1800931 (2018).
1092 51. Shaffer, S. A. *et al.* In vitro and in vivo metabolism of paclitaxel poliglumex:
1093 identification of metabolites and active proteases. *Cancer Chemother. Pharmacol.* **59**,
1094 537–548 (2007).
1095 52. Gordon, S. R. *et al.* PD-1 expression by tumour-associated macrophages inhibits
1096 phagocytosis and tumour immunity. *Nature* **545**, 495–499 (2017).
1097 53. Zhang, M. *et al.* Anti-CD47 Treatment Stimulates Phagocytosis of Glioblastoma by
1098 M1 and M2 Polarized Macrophages and Promotes M1 Polarized Macrophages In Vivo.
1099 *PLOS ONE* **11**, e0153550 (2016).
1100 54. Simon-Gracia, L. *et al.* Bifunctional Therapeutic Peptides for Targeting Malignant B
1101 Cells and Hepatocytes: Proof of Concept in Chronic Lymphocytic Leukemia. *Adv. Ther.* **3**,
1102 2000131 (2020).

1103 55. MPD: Phenotype strain survey measures: alanine aminotransferase.
1104 https://phenome.jax.org/search/details/ssmeasures?searchterm=alanine+aminotransferase+
1105 &ontavail=2.
1106 56. BALB/c Mouse | Charles River Laboratories. https://www.criver.com/products-
1107 services/find-model/balbc-mouse?region=3616.
1108 57. Cassetta, L. & Kitamura, T. Targeting Tumor-Associated Macrophages as a Potential
1109 Strategy to Enhance the Response to Immune Checkpoint Inhibitors. *Front. Cell Dev. Biol.*
1110 **0**, (2018).
1111 58. Santoni, M. *et al.* Triple negative breast cancer: Key role of Tumor-Associated
1112 Macrophages in regulating the activity of anti-PD-1/PD-L1 agents. *Biochim. Biophys. Acta*
1113 *BBA - Rev. Cancer* **1869**, 78–84 (2018).
1114 59. Rodell, C. B. *et al.* TLR7/8-agonist-loaded nanoparticles promote the polarization of
1115 tumour-associated macrophages to enhance cancer immunotherapy. *Nat. Biomed. Eng.* **2**,
1116 578–588 (2018).
1117 60. Loeuillard, E. *et al.* Targeting tumor-associated macrophages and granulocytic
1118 myeloid-derived suppressor cells augments PD-1 blockade in cholangiocarcinoma. *J. Clin.*
1119 *Invest.* **130**, 5380–5396 (2020).
1120 61. Choo, Y. W. *et al.* M1 Macrophage-Derived Nanovesicles Potentiate the Anticancer
1121 Efficacy of Immune Checkpoint Inhibitors. *ACS Nano* **12**, 8977–8993 (2018).
1122 62. Arlauckas, S. P. *et al.* Arg1 expression defines immunosuppressive subsets of tumor-
1123 associated macrophages. *Theranostics* **8**, 5842–5854 (2018).
1124 63. Landry, A. P., Balas, M., Alli, S., Spears, J. & Zador, Z. Distinct regional ontogeny
1125 and activation of tumor associated macrophages in human glioblastoma. *Sci. Rep.* **10**,
1126 19542 (2020).

1127 64. Zheng, X. *et al.* Spatial Density and Distribution of Tumor-Associated Macrophages
1128 Predict Survival in Non–Small Cell Lung Carcinoma. *Cancer Res.* **80**, 4414–4425 (2020).
1129 65. Viitala, M. *et al.* Immunotherapeutic Blockade of Macrophage Clever-1 Reactivates
1130 the CD8 $^{+}$ T-cell Response against Immunosuppressive Tumors. *Clin. Cancer Res.* **25**,
1131 3289–3303 (2019).
1132 66. Etzerodt, A. *et al.* Specific targeting of CD163+ TAMs mobilizes inflammatory
1133 monocytes and promotes T cell–mediated tumor regression. *J. Exp. Med.* **216**, 2394–2411
1134 (2019).
1135 67. Linde, N. *et al.* Macrophages orchestrate breast cancer early dissemination and
1136 metastasis. *Nat. Commun.* **9**, 1–14 (2018).
1137 68. Witschen, P. M. *et al.* Tumor Cell Associated Hyaluronan-CD44 Signaling Promotes
1138 Pro-Tumor Inflammation in Breast Cancer. *Cancers* **12**, 1325 (2020).
1139 69. Guo, C. *et al.* Liposomal Nanoparticles Carrying anti-IL6R Antibody to the Tumour
1140 Microenvironment Inhibit Metastasis in Two Molecular Subtypes of Breast Cancer Mouse
1141 Models. *Theranostics* **7**, 775–788 (2017).
1142 70. Movahedi, K. *et al.* Nanobody-Based Targeting of the Macrophage Mannose
1143 Receptor for Effective *In Vivo* Imaging of Tumor-Associated Macrophages. *Cancer Res.*
1144 **72**, 4165–4177 (2012).
1145 71. Azad, A. K. *et al.* γ-Tilmanocept, a New Radiopharmaceutical Tracer for Cancer
1146 Sentinel Lymph Nodes, Binds to the Mannose Receptor (CD206). *J. Immunol.* **195**, 2019–
1147 2029 (2015).
1148 72. Jaynes, J. M., Lopez, H. W., Martin, G. R., YATES, C. & Garvin, C. E. Peptides
1149 having anti-inflammatory properties. (2016).
1150 73. Scodeller, P. & Asciutto, E. K. Targeting Tumors Using Peptides. *Molecules* **25**, 808
1151 (2020).

1152 74. Ekladious, I., Colson, Y. L. & Grinstaff, M. W. Polymer–drug conjugate therapeutics:
1153 advances, insights and prospects. *Nat. Rev. Drug Discov.* **18**, 273–294 (2019).
1154 75. Duro-Castano, A., Conejos-Sánchez, I. & Vicent, M. J. Peptide-Based Polymer
1155 Therapeutics. *Polymers* **6**, 515–551 (2014).
1156 76. Moura, L. I. F. *et al.* Functionalized branched polymers: promising
1157 immunomodulatory tools for the treatment of cancer and immune disorders. *Mater. Horiz.*
1158 **6**, 1956–1973 (2019).
1159 77. Melnyk, T., Đorđević, S., Conejos-Sánchez, I. & Vicent, M. J. Therapeutic potential
1160 of polypeptide-based conjugates: Rational design and analytical tools that can boost
1161 clinical translation. *Adv. Drug Deliv. Rev.* **160**, 136–169 (2020).
1162 78. Duro-Castano, A. *et al.* Capturing "Extraordinary" Soft-Assembled Charge-Like
1163 Polypeptides as a Strategy for Nanocarrier Design. *Adv. Mater.* **29**, 1702888 (2017).
1164 79. Duro-Castano, A., Movellan, J. & Vicent, M. J. Smart branched polymer drug
1165 conjugates as nano-sized drug delivery systems. *Biomater. Sci.* **3**, 1321–1334 (2015).
1166 80. Cortez-Retamozo, V. *et al.* Origins of tumor-associated macrophages and neutrophils.
1167 *Proc. Natl. Acad. Sci.* **109**, 2491–2496 (2012).
1168 81. Kurashige, M. *et al.* Origin of cancer-associated fibroblasts and tumor-associated
1169 macrophages in humans after sex-mismatched bone marrow transplantation. *Commun.*
1170 *Biol.* **1**, 1–13 (2018).
1171 82. Veglia, F. & Gabrilovich, D. I. Dendritic cells in cancer: the role revisited. *Curr.*
1172 *Opin. Immunol.* **45**, 43–51 (2017).
1173 83. Agostinis, P. *et al.* PHOTODYNAMIC THERAPY OF CANCER: AN UPDATE.
1174 *CA. Cancer J. Clin.* **61**, 250–281 (2011).

1175 84. Cheah, H. Y. *et al.* Near-Infrared Activatable Phthalocyanine–Poly-L-Glutamic Acid
1176 Conjugate: Enhanced in Vivo Safety and Antitumor Efficacy toward an Effective
1177 Photodynamic Cancer Therapy. *Mol. Pharm.* **15**, 2594–2605 (2018).
1178 85. Nguyen, V.-N., Yan, Y., Zhao, J. & Yoon, J. Heavy-Atom-Free Photosensitizers:
1179 From Molecular Design to Applications in the Photodynamic Therapy of Cancer. *Acc.*
1180 *Chem. Res.* **54**, 207–220 (2021).
1181 86. Tacar, O., Sriamornsak, P. & Dass, C. R. Doxorubicin: an update on anticancer
1182 molecular action, toxicity and novel drug delivery systems. *J. Pharm. Pharmacol.* **65**,
1183 157–170 (2013).
1184 87. Shan, H., Dou, W., Zhang, Y. & Qi, M. Targeted ferritin nanoparticle encapsulating
1185 CpG oligodeoxynucleotides induces tumor-associated macrophage M2 phenotype
1186 polarization into M1 phenotype and inhibits tumor growth. *Nanoscale* **12**, 22268–22280
1187 (2020).
1188 88. Ramesh, A., Brouillard, A., Kumar, S., Nandi, D. & Kulkarni, A. Dual inhibition of
1189 CSF1R and MAPK pathways using supramolecular nanoparticles enhances macrophage
1190 immunotherapy. *Biomaterials* **227**, 119559 (2020).
1191 89. Hollmén, M. *et al.* G-CSF regulates macrophage phenotype and associates with poor
1192 overall survival in human triple-negative breast cancer. *OncoImmunology* **5**, e1115177
1193 (2016).
1194 90. Georgoudaki, A.-M. *et al.* Reprogramming Tumor-Associated Macrophages by
1195 Antibody Targeting Inhibits Cancer Progression and Metastasis. *Cell Rep.* **15**, 2000–2011
1196 (2016).
1197 91. Zhang, F. *et al.* Reprogramming of profibrotic macrophages for treatment of
1198 bleomycin-induced pulmonary fibrosis. *EMBO Mol. Med.* **12**, e12034 (2020).

1199 92. Sartor, O. *et al.* Lutetium-177–PSMA-617 for Metastatic Castration-Resistant
1200 Prostate Cancer. *N. Engl. J. Med.* **0**, null (2021).
1201 93. Tian, C. *et al.* ff19SB: Amino-Acid-Specific Protein Backbone Parameters Trained
1202 against Quantum Mechanics Energy Surfaces in Solution. *J. Chem. Theory Comput.* **16**,
1203 528–552 (2020).
1204 94. AmberTools - SBGrid Consortium - Supported Software.
1205 https://sbgrid.org/software/titles/ambertools.
1206 95. Hopkins, C. W., Le Grand, S., Walker, R. C. & Roitberg, A. E. Long-Time-Step
1207 Molecular Dynamics through Hydrogen Mass Repartitioning. *J. Chem. Theory Comput.*
1208 **11**, 1864–1874 (2015).
1209 96. Berendsen, H. J. C., Postma, J. P. M., van Gunsteren, W. F., DiNola, A. & Haak, J. R.
1210 Molecular dynamics with coupling to an external bath. *J. Chem. Phys.* **81**, 3684–3690
1211 (1984).
1212 97. Ryckaert, J.-P., Ciccotti, G. & Berendsen, H. J. C. Numerical integration of the
1213 cartesian equations of motion of a system with constraints: molecular dynamics of n-
1214 alkanes. *J. Comput. Phys.* **23**, 327–341 (1977).
1215 98. Ray, A. & Dittel, B. N. Isolation of Mouse Peritoneal Cavity Cells. *J. Vis. Exp. JoVE*
1216 1488 (2010) doi:10.3791/1488.
1217 99. Bankhead, P. *et al.* QuPath: Open source software for digital pathology image
1218 analysis. *Sci. Rep.* **7**, 16878 (2017).
1219

1220 **ACKNOWLEDGEMENTS**

1221 We would like to thank Stuart P. Atkinson for English editing, Merje Jakobson for performing
1222 H&E studies on paraffin-embedded formalin-fixed tissues, Dr. Aivar Orav for in vivo toxicity
1223 study analysis and Dr. Mario Plaas for the help with the slide scanner. PS acknowledges support
1224 from the Estonian Research Council (grant: PUT PSG38 to PS) and a Feasibility fund of the
1225 University of Tartu (grant: ARENG51 to PS). AL acknowledges a PhD fellowship from the

Estonian government. MJV acknowledges the support by European Research Council grants (ERC-CoG-2014-648831 “My-Nano” and ERC-PoC-2018-825798 “Polymmune”). Part of the equipment employed in this work has been funded by Generalitat Valenciana and co-financed with FEDER funds (PO FEDER of Comunitat Valenciana 2014−2020). UH acknowledges the support by EsRC Mobilitas+ grant MOBTP185. TT acknowledges the support by UT EIK grant and GMVBS0230PR.

AUTHOR CONTRIBUTIONS

AL performed the in vitro and in vivo experiments, histology, immunofluorescence, flow cytometry, analysis and wrote the manuscript. AM performed chemical design, synthesis, and characterisation and edited the manuscript. UH performed flow cytometry experiments and analysis. EA, MP, and MB performed computational simulations. SD performed drug release studies and chemical characterisation. LS performed analysis and expert evaluation of H&E images. PP edited the manuscript and provided discussions and lab support. TT edited the manuscript, participated in the experimental design and discussions, and provided laboratory support. MJV performed chemical design, in vitro and in vivo experiment design, supervised chemical synthesis and characterisation, provided lab support, and edited the manuscript. PS supervised all the experiments, participated in their design and analysis, and edited the manuscript. All authors edited the manuscript and approved the final version.

CORRESPONDING AUTHORS

Correspondence to Tambet Teesalu, María J. Vicent and Pablo Scodeller.

CONFLICT OF INTERESTS

PS and TT are inventors of patents on the mUNO peptide. MJV is an inventor of a patent on BTA-core branched polypeptides (including St-PGA) licensed to PTS SL. In addition, TT is an inventor of iRGD and CendR peptides and a shareholder of Cend Therapeutics Inc., a company that holds a license for the mUNO, iRGD and CendR peptides.